ANNUAL REVIEWS

Annual Review of Astronomy and Astrophysics

First Multimessenger Observations of a Neutron Star Merger

Raffaella Margutti[1,2] and Ryan Chornock[1,2,3]

[1]Department of Astronomy, University of California, Berkeley, California 94720, USA;
email: rmargutti@berkeley.edu, chornock@berkeley.edu

[2]Center for Interdisciplinary Exploration and Research in Astrophysics (CIERA) and Department of Physics and Astronomy, Northwestern University, Evanston, Illinois 60208, USA

[3]Astrophysical Institute, Department of Physics and Astronomy, Ohio University, Athens, Ohio 45701, USA

Annu. Rev. Astron. Astrophys. 2021. 59:155–202

First published as a Review in Advance on June 3, 2021

The *Annual Review of Astronomy and Astrophysics* is online at astro.annualreviews.org

https://doi.org/10.1146/annurev-astro-112420-030742

Keywords

gravitational wave sources, jets, nucleosynthesis, relativistic binary stars, transient sources

Abstract

We describe the first observations of the same celestial object with gravitational waves and light.

- GW170817 was the first detection of a neutron star merger with gravitational waves.
- The detection of a spatially coincident weak burst of gamma-rays (GRB 170817A) 1.7 s after the merger constituted the first electromagnetic detection of a gravitational wave source and established a connection between at least some cosmic short gamma-ray bursts (SGRBs) and binary neutron star mergers.
- A fast-evolving optical and near-infrared transient (AT 2017gfo) associated with the event can be interpreted as resulting from the ejection of $\sim$0.05 $M_\odot$ of material enriched in r-process elements, finally establishing binary neutron star mergers as at least one source of r-process nucleosynthesis.

- Radio and X-ray observations revealed a long-rising source that peaked ~160 d after the merger. Combined with the apparent superluminal motion of the associated very long baseline interferometry source, these observations show that the merger produced a relativistic structured jet whose core was oriented ≈20 deg from the line of sight and with properties similar to SGRBs. The jet structure likely results from interaction between the jet and the merger ejecta.
- The electromagnetic and gravitational wave information can be combined to produce constraints on the expansion rate of the Universe and the equation of state of dense nuclear matter. These multimessenger endeavors will be a major emphasis of future work.

Contents

1. INTRODUCTION

Disparate threads of research from astrophysics, general relativity, and nuclear physics were united on August 17, 2017, with the discovery of GW170817 by the Advanced Laser Interferometer Gravitational-wave Observatory (LIGO; Aasi et al. 2015) and Advanced Virgo (Acernese et al. 2015) interferometers. A gravitational wave (GW) source with a signal indicative of a compact binary merger (Abbott et al. 2017f) was followed by a short γ-ray burst (SGRB; Goldstein et al. 2017, Savchenko et al. 2017) and an optical counterpart localized to the outskirts of the nearby galaxy NGC 4993 (Coulter et al. 2017). The intensive campaign across the electromagnetic (EM) spectrum to characterize the source (Abbott et al. 2017a) was a watershed event in astrophysics, marking the first multimessenger detection of a binary neutron star (BNS) merger. Here, we review the observations of this event and summarize the key inferences that followed.

1.1. Thread 1: Gravitational Wave Sources and Neutron Star Mergers

Ever since the discovery of PSR 1913+16 (Hulse & Taylor 1975), it has been known that compact object binaries exist in our Galaxy, and that at least some of them will decay by emission of GWs to merge in less than a Hubble time (Taylor & Weisberg 1982). Current estimates are that the rate of BNS mergers in the Galaxy is $\mathfrak{R}_{\rm BNS} = 37^{+24}_{-11}$ Myr^{-1} (90% confidence level or c.l.; Pol et al. 2020). The existence of GW emission from compact object binaries was spectacularly confirmed by the detection of the binary black hole (BH) system GW150914 (Abbott et al. 2016).

What happens in a merger when one of the compact objects is a neutron star (NS)? Lattimer & Schramm (1974) first considered NS–BH mergers and found that ∼5% of the NS material might be ejected. This idea was soon extended to BNS mergers (Symbalisty & Schramm 1982, Eichler et al. 1989). Simulations have grown in numerical sophistication over the past few decades and identified several possible mass ejection mechanisms in BNS mergers (Rosswog et al. 1999, Oechslin et al. 2007, Bauswein et al. 2013, Hotokezaka et al. 2013). In the last few orbits before the merger occurs, the NSs are tidally squeezed and eject tidal tails of decompressed NS material (e.g., Sekiguchi et al. 2016). Further dynamic ejection of matter occurs at the collision interface between the two NSs (e.g., Wanajo et al. 2014). Up to 0.1 $M_\odot$ of material can then form a disk around the remnant compact object (Radice et al. 2018a). Winds and outflows driven from either a hypermassive NS (HMNS) remnant or the disk surface can be powered by neutrinos, magnetic fields, or viscous effects, resulting in enhanced mass loss (see Section 8.2; Dessart et al. 2009, Metzger & Fernández 2014, Perego et al. 2014, Siegel et al. 2014).

Hypermassive NS (HMNS): neutron star with $M > M_{\rm TOV}$ and $M > M^{\rm NS}_{\rm rot}$, which is temporarily stabilized against gravitational collapse for ∼1 s by differential rotation and thermal gradients

The dynamics of the merger process and mass ejection have been reviewed recently by Shibata & Hotokezaka (2019) and Radice et al. (2020).

1.2. Thread 2: The Mystery of the *r*-Process

Nuclei of elements heavier than the iron peak are primarily formed through neutron capture reactions. Burbidge et al. (1957) and Cameron (1957) identified two separate processes that were necessary to produce the measured isotopic ratios of the heavy elements in the Solar System (Suess & Urey 1956). The key distinction is whether the timescale between successive neutron captures is substantially shorter or longer than the beta decay timescales of the unstable nuclei that form. Although the slow *s*-process has been conclusively shown to occur in evolved stars, the site(s) of the rapid *r*-process has been debated for more than 60 years (e.g., Sneden et al. 2008, Cowan et al. 2019). In parallel with these debates, significant constraints were provided by studies of the abundances of neutron capture elements in extremely metal-poor stars (e.g., Frebel 2018). They have shown that the abundance ratios for the heaviest *r*-process elements (Ba and higher) were very close to those seen in the Sun, whereas the lighter *r*-process elements exhibited significantly higher scatter from star to star. The initial suggestion was that supernovae (SNe) and the vicinities of the newly formed NSs in their interiors provided the hot, neutron-rich environments favorable for the *r*-process. However, detailed numerical simulations of the resulting nucleosynthesis have generally failed to reliably produce the heaviest elements in sufficient abundance (e.g., Qian & Woosley 1996).

The neutron-rich ejecta of NS–BH mergers were suggested to be interesting potential sites for *r*-process nucleosynthesis (Lattimer & Schramm 1974, 1976), as were BNS systems (Symbalisty & Schramm 1982, Eichler et al. 1989). Detailed nucleosynthesis calculations of BNS mergers supported the idea that they might result in significant *r*-process production (Freiburghaus et al. 1999, Rosswog et al. 1999). An important parameter is the electron fraction, Y_e, which is the ratio of the number of protons to nucleons in the ejecta material. Low Y_e material is neutron rich and can experience the *r*-process. However, doubts remained about whether the event rates or ejecta masses were sufficiently high to contribute significantly to Galactic nucleosynthesis (e.g., Qian & Wasserburg 2007). Nonetheless, circumstantial evidence from such disparate lines of evidence as low ^{244}Pu abundances in the ocean floor (Hotokezaka et al. 2015, Wallner et al. 2015) and a large *r*-process enhancement in the chemical abundances of the dwarf galaxy Reticulum II (Ji et al. 2016) accumulated and pointed to rare events with large yields being responsible for the majority of *r*-process production, particularly for the heaviest neutron-capture elements, which was hard to accommodate in SN models. Resolution of the *r*-process mystery would also give insight into the nuclear physics of neutron-rich isotopes, only some of which are currently experimentally accessible (Mumpower et al. 2016, Horowitz et al. 2019).

1.3. Thread 3: Short Gamma-Ray Bursts

SGRBs are cosmic flashes of γ-rays (Klebesadel et al. 1973) with durations of less than 2 s (Kouveliotou et al. 1993). Circumstantial observational evidence of the association of SGRBs with mergers of compact objects (either NS–NS or NS–BH) has been reviewed by Berger (2014) and includes very deep optical observations that rule out the presence of SN explosions; observed optical/near-infrared (NIR) excesses of emission with respect to the afterglow decay, detected in some nearby SGRBs with properties consistent with *r*-process-powered kilonovae; and the remote locations of SGRBs in their host galaxies, which are of early-type morphology in ∼1/3 of events, which is indicative of older stellar populations. Additionally, the location of SGRBs within their host galaxies is weakly correlated with the underlying host-galaxy light distribution, indicating that SGRBs are not good tracers of star formation or stellar mass. These indirect pieces of evidence collectively favor NS–NS and/or NS–BH mergers as progenitors of SGRBs, as was theoretically postulated by Eichler et al. (1989) and Narayan et al. (1992). Yet, before GW170817, no direct observational evidence supported this conclusion.

1.4. A (Brief) Overview of Electromagnetic Counterpart Predictions

Prior to GW170817, EM counterparts to NS mergers detected through GWs had been proposed across the spectrum from γ-rays to radio, with a range of timescales from seconds to years (see the review by Fernández & Metzger 2016). The odds that the narrow γ-ray-emitting relativistic jet would be aimed directly at the observer were regarded as low for any individual event, despite the importance of making such a connection (Metzger & Berger 2012). This motivated a focus on more isotropic signatures for counterpart searches.

Li & Paczyński (1998) realized that the combination of NS merger ejecta unbound to the final compact object with a source of energy from radioactive decays should result in an observable optical transient, although they predicted high luminosities ($L_{\rm peak} \approx 10^{44}$ erg s^{-1}) and short durations (~1 day). These events were sometimes referred to as mini-SNe. Kulkarni (2005) considered counterparts powered by decay of free neutrons or nickel and introduced the term macronova. The first models to incorporate more realistic treatments of radioactive heating and thermalization by r-process decay products assumed simplified opacities inspired by Thomson scattering and iron-peak elements (Metzger et al. 2010, Goriely et al. 2011, Roberts et al. 2011). As the significantly lower predicted luminosities of $L_{\rm peak} \approx 10^{41}$–$10^{42}$ erg s^{-1} were approximately 1,000× those of classical novae, Metzger et al. (2010) coined the term kilonova for these transients, which we adopt here.

A major theoretical breakthrough was provided by considerations of the opacities of lanthanide elements, which are copiously produced by the strong r-process (Kasen et al. 2013). Atoms and ions whose valence electrons partially fill the f-shell have a substantially larger number of low-lying energy levels and, hence, bound–bound transitions available to them than iron-peak elements. This dramatically increases the opacity of lanthanide-rich material at optical wavelengths, which delays and lowers the peak luminosity of a kilonova and pushes flux to emerge in the NIR, which we refer to as a red kilonova (Barnes & Kasen 2013, Kasen et al. 2013, Tanaka & Hotokezaka 2013). Later, it was realized that lanthanide-poor material ejected with high Y_e, potentially from polar dynamical ejecta or winds, could produce a blue kilonova that dominates the optical emission (Metzger & Fernández 2014). The histories of kilonova predictions and evolving input physics have been comprehensively reviewed by Metzger (2019). Nakar & Piran (2011) also predicted that the kilonova ejecta would emit synchrotron radiation as they decelerate in the ambient medium to produce a detectable radio counterpart to BNS mergers on timescales of years.

A solid prediction from the numerical simulations described above is that the merger site is surrounded by some baryon contaminated region with large mass ($\gtrsim$0.01 $M_\odot$). An SGRB-like jet launched by the merger would thus have to pierce through these outflows of material before breaking out. Before GW170817 it was realized that the jet propagation within the BNS ejecta is a critical step that shapes the jet's final angular structure and collimation, and that determines its ultimate fate (successful versus choked; e.g., Aloy et al. 2005, Bromberg et al. 2011, Nagakura et al. 2014, Duffell et al. 2015, Lazzati et al. 2017a, Murguia-Berthier et al. 2017b, Nakar & Piran 2017, Gottlieb et al. 2018a). While advancing through the ejecta, the jet dissipates energy into a hot cocoon (i.e., a wide-angle outflow constituted of shocked jet and ejecta material), which expands relativistically after breaking out of the ejecta. Numerical simulations suggest that for standard parameters of successful jets, the time spent by the jet within the BNS ejecta is comparable with the duration of the subsequent SGRB γ-ray emission, implying that the cocoon energy and the γ-ray burst (GRB) energy are expected to be similar. Just like the jet, the cocoon has clear EM signatures associated with it, including cocoon breakout γ-ray emission, ultraviolet (UV) cooling emission, radioactive heating, and a broadband afterglow. None of these cocoon observational signatures were confidently detected in SGRBs before GW170817, and some still remain elusive (Sections 3–5).

1.5. The Events of August 17, 2017

A GW signal was detected as a compact binary coalescence by Advanced LIGO and Advanced Virgo on August 17, 2017, with the end of the inspiral signal at 12:41:04.4 UTC (after ~100 s of GW emission detectable in the LIGO band; Abbott et al. 2017f). This event was followed 1.74 ± 0.05 s later by a burst of γ-rays detected by the *Fermi* Gamma-ray Burst Monitor (*Fermi*-GBM; Goldstein et al. 2017) and INTEGRAL SPI-ACS (the anti-coincidence system of spectrometer SPI on the *International Gamma-Ray Astrophysics Laboratory*; Savchenko et al. 2017). The subsequent detection of an optical counterpart to GW170817 and GRB 170817A was first made by the One-Meter Two-Hemispheres collaboration using the Swope Telescope at 10.9 h after the merger (Coulter et al. 2017), and within the next hour five other teams independently detected the same source, now known as AT 2017gfo (see the sidebar titled Nomenclature; Arcavi et al. 2017, Lipunov et al. 2017, Soares-Santos et al. 2017, Tanvir et al. 2017, Valenti et al. 2017). No X-ray or radio counterpart was detected down to deep limits during the first few days of observations (Alexander et al. 2017, Evans et al. 2017, Hallinan et al. 2017, Margutti et al. 2017, Savchenko et al. 2017, Sugita et al. 2018). A rising X-ray and radio source eventually crossed the threshold of detection of sensitive X-ray (*Chandra X-ray Observatory*) and radio (VLA, or the Very Large Array) observatories on day 8.9 (Troja et al. 2017) and day 16.4 (Hallinan et al. 2017) of monitoring, respectively (with a tentative radio detection at $\delta t = 10.4$ days). Abbott et al. (2017a) give a detailed account of the time line of EM observations that followed the initial detection of the GW source. Multimessenger observations of GW170817 and their implications have also been reviewed by Nakar (2019) and Burns (2019).

Several different techniques give redshift-independent distance estimates of ~40 Mpc for the host galaxy NGC 4993 (e.g., Hjorth et al. 2017). Here, we adopt $D_{\rm L} = 40.7 \pm 1.4 \pm 1.9$ Mpc (random and systematic uncertainties, respectively) obtained from surface brightness fluctuations in NGC 4993 (Cantiello et al. 2018). Time is referenced to the GW coalescence time, 2017-08-17 12:41:04.4 UTC (or MJD = 57982.528523; Abbott et al. 2017f). All photometry and spectroscopy in the figures have been corrected for $E(B - V) = 0.105$ mag of Galactic reddening (Schlafly & Finkbeiner 2011). We adopt the MUSE (Multi Unit Spectroscopic Explorer)/Very Large Telescope measurement of the heliocentric redshift of NGC 4993 $z_{\rm helio} = 0.0098$ (Hjorth et al. 2017, Levan et al. 2017), which gives a geocentric redshift of $z = 0.0099$ at the time of GW170817. All

NOMENCLATURE

The EM counterpart to GW170817 has been referred to by several equivalent names in the literature: SSS17a (Coulter et al. 2017), DLT17ck (Valenti et al. 2017), MASTER OTJ130948.10-232253.3 (Lipunov et al. 2017), and EM170817 (e.g., Evans et al. 2017, Kasliwal et al. 2017b). We adopt the official International Astronomical Union transient name, AT 2017gfo, in this review for the thermal UV–optical–IR source. When speaking specifically of the burst of γ-rays, which was automatically labeled GRB 170817A, we follow the convention from that community. We refer to the GW event as GW170817, and to the associated nonthermal emission as synchrotron emission from the afterglow of GW170817.

quoted magnitudes are on the AB system. Uncertainties (upper limits) are provided at the 1σ (3σ) Gaussian-equivalent confidence level unless explicitly mentioned otherwise.

2. GW170817: GRAVITATIONAL WAVE EMISSION

The GW signal of GW170817 was detected at high significance in both the Advanced LIGO-Hanford and LIGO-Livingston detectors (combined signal-to-noise ratio of 32.4 with a false alarm rate of less than one in 8×10^4 years; Abbott et al. 2017f), despite a detector glitch in the LIGO-Livingston detector that appeared 1.1 s prior to coalescence. This event only resulted in a signal-to-noise ratio of ∼2 in the Virgo detector, which is surprisingly low given the proximity of the event, and which implied a localization near the detector nulls. The luminosity distance estimate was $D_L = 40^{+8}_{-14}$ Mpc and the sky map had a 90% GW localization region of 28 deg^2 (Abbott et al. 2017f), which was later reduced to 16 deg^2 after reanalysis (Abbott et al. 2019a). Both regions include the sky location of AT 2017gfo, and the GW localization volume includes its host galaxy, NGC 4993 (see **Figure 1**).

Chirp mass ($\mathcal{M}$): $\mathcal{M} \equiv \frac{(m_1 m_2)^{3/5}}{(m_1+m_2)^{1/5}}$; the best-measured parameter from the modeling of GW sources having a long inspiral

Dimensionless spin (χ_i): $\chi_i \equiv \frac{c\mathcal{S}_i}{(Gm_i^2)}$, where $\mathcal{S}_i$ is the spin angular momentum vector of the ith component of the binary

Binary inclination angle (θ_{JN}): angle between the binary angular momentum and the observer's line of sight

2.1. Source Parameters and Basic Inferences

The physical properties of GW sources are inferred by matching the observed data with waveforms generated following the prescriptions of general relativity (GR), which makes detailed predictions for the inspiral and coalescence signal of merging NSs and BHs. The observed waveform depends on a combination of intrinsic and extrinsic parameters. Intrinsic parameters include the component masses m_1 and m_2 (and their notable combinations, i.e., mass ratio $q \equiv m_2/m_1 \leq 1$ and chirp mass, $\mathcal{M}$), spin angular momenta of the two bodies that contribute six parameters $\mathcal{S}_i$ (typically expressed in terms of dimensionless spin, χ_i), and parameters governing the tidal deformability of each binary component. Extrinsic parameters are those related to the localization of the GW event in the sky, the luminosity distance, and the orientation of the binary angular momentum with respect to the observer, i.e., the binary inclination angle (θ_{JN}). The constraints on the deformability of matter derived from this system are discussed in Section 6.1. Here, we focus on the component masses and spins.

A first estimate of these parameters was presented by Abbott et al. (2017f). Abbott et al. (2019a) present more precise parameter constraints that primarily result from the reduced calibration uncertainties of Virgo data, a broader bandwidth of GW data included in the analysis (extending to 23 Hz compared to the 30 Hz of the original analysis by Abbott et al. 2017f, which gives access to an additional ∼1,500 cycles out of a total of ∼3,000), a wider range of improved waveform models, and knowledge of the source location within NGC 4993 from EM observations. By making minimal assumptions about the nature of the merging compact objects and, specifically, by allowing for a large range of deformabilities that include the possibility of BH components, Abbott et al. (2019a) derive a primary mass $m_1 \in (1.36, 1.89)\,M_\odot$ (one-sided, 90% lower and upper limits), a secondary mass $m_2 \in (1.00, 1.36)\,M_\odot$, and a total mass of $2.77^{+0.22}_{-0.05}\,M_\odot$ (median, 5% lower limit and 95% upper limit) enforcing a prior $\chi \leq 0.89$. Individual components' spins are less well constrained to $\chi_1 \in (0.00, 0.50)$ and $\chi_2 \in (0.00, 0.61)$. The mass values are consistent with being drawn from the Galactic NS population (which is described by a mean value of $m_{MW} = 1.32\,M_\odot$ with standard deviation $\sigma_{MW} = 0.11\,M_\odot$; Kiziltan et al. 2013), yet this comparison does not imply that GW170817 contained NSs (Section 6.1). The detection of EM emission (Sections 4 and 5), however, does imply that at least one of the merging compact objects is an NS.

The fastest-spinning Galactic BNSs that will merge within a Hubble time have an extrapolated $\chi \leq 0.04$ at the time of merger. A low-spin prior $\chi \leq 0.05$ consistent with this known Galactic

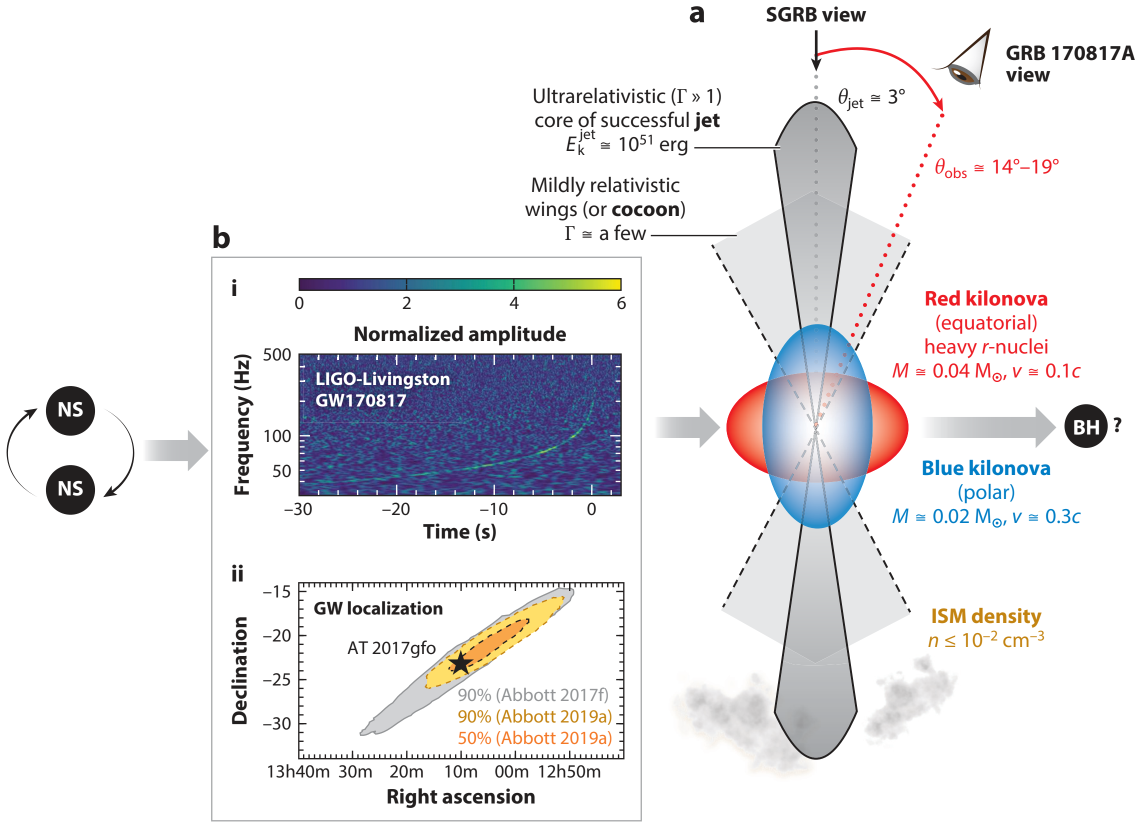

Figure 1

Schematic (*a*) and composite panel (*b*) showing the EM+GW emission components and geometry of the compact-object merger GW170817. The GW emission was detectable until the merger time [$t = 0$ in the time-frequency representation (*b*, subpanel *i*) of the LIGO-Livingston data], and enabled an initial localization within 28 deg^2 (Abbott et al. 2017f), which was later refined to 16 deg^2 (Section 2; Abbott et al. 2019a). (*b*, subpanel *ii*) The merger produced a burst of γ-rays (GRB 170817A; Section 3), and a multiwavelength afterglow powered by a collimated relativistic jet with a wider-angle component of mildly relativistic material viewed off axis (Section 5). A multicolor kilonova dominated the UV–optical–NIR spectrum for the first weeks (Section 4). Although the ultimate fate of the merger remnant cannot be probed directly, indirect evidence favors a BH (Section 8.2). Panel *b*, subpanel *i*, adapted from Abbott et al. 2017f. Abbreviations: BH, black hole; EM, electromagnetic; GW, gravitational wave; ISM, interstellar medium; NIR, near-infrared; NS, neutron star; SGRB, short γ-ray burst; UV, ultraviolet.

population leads to $m_1 \in (1.36, 1.60)\,M_\odot$, $m_2 \in (1.16, 1.36)\,M_\odot$, and total mass $2.73^{+0.04}_{-0.01}\,M_\odot$. As expected, in both spin scenarios, the chirp mass is derived with much higher precision, $\mathcal{M} = 1.186^{+0.001}_{-0.001}\,M_\odot$, with the main source of uncertainty contributing to the quoted error bars being the unknown source velocity in NGC 4993 (which is quantified by the observed line-of-sight velocity dispersion of NGC 4993). Finally, the GW analysis points at a binary system that is inclined with respect to the observer's line of sight of $\theta_{JN} = 151\ \mathrm{deg}^{+15}_{-11}$ ($\theta_{JN} = 153\ \mathrm{deg}^{+15}_{-11}$) for the low-spin (high-spin) prior after using the D_L measurement from EM observations of the host galaxy (see Section 6.2). All parameter ranges and uncertainties are quoted following the 90% convention above. Adding more informative priors that are astrophysically motivated and assuming that both objects are NSs have minimal impact on the individual mass estimates, but enable tighter constraints on the deformability of matter (in Section 6.1; Abbott et al. 2018).

3. GRB 170817A: GAMMA-RAY EMISSION

The burst of γ-rays detected by *Fermi*-GBM (Goldstein et al. 2017), and by INTEGRAL SPI-ACS (Savchenko et al. 2017) at $\Delta t_{\text{GW-}\gamma} = 1.74 \pm 0.05$ s after the binary coalescence and spatially coincident with the GW localization of the BNS merger GW170817, represents the first EM signature physically associated with a GW source (probability of chance coincidence of 5×10^{-8}, or 5.8σ Gaussian equivalent; Abbott et al. 2017b) and marks the dawn of multimessenger astrophysics with GWs. The key observational properties of the γ-ray counterpart to GW170817 are as follows (Goldstein et al. 2017; see also Pozanenko et al. 2018, Fraija et al. 2019): The *Fermi*-GBM light curve of GRB 170817A showed a peculiar morphology consisting of a spike of emission of ∼0.5 s (also detected by INTEGRAL) followed by a lower-significance tail of softer emission, with total duration of $T_{90} = 2.0 \pm 0.5$ s (**Figure 2**). The spectrum of the short spike is well fitted by a power law with exponential cutoff (i.e., a Comptonized model) with peak energy of the νF_ν spectrum $E_{\text{peak}} = 185 \pm 62$ keV and isotropic equivalent energy release $E_{\gamma,\text{iso}} = (3.6 \pm 0.9) \times 10^{46}$ erg (10–1,000 keV). The spectrum of the softer tail can be fitted with a blackbody model with temperature $T = 10.3 \pm 1.5$ keV and $E_{\gamma,\text{iso}} = (1.2 \pm 0.3) \times 10^{46}$erg, even if the limited photon statistics prevent any conclusive statement about the nature of the intrinsic spectrum. GRB 170817A showed no evidence for a γ-ray precursor or extended emission (EE).

Extended emission (EE): period of up to ∼100 s of enhanced γ-ray activity after the short γ-ray spike that can be energetically dominant (as in SGRB 080503)

Observer angle (θ_{obs}): the minimum between θ_{JN} and (180 deg − θ_{JN}) if the jet is launched along the direction of the angular momentum

The fact that GRB 170817A is significantly less energetic than cosmological SGRBs (**Figure 2**) is not surprising, as the most likely scenario of GW-detected BNS mergers is that of an off-axis configuration (typical observer angle $\theta_{\text{obs}} \sim 30$ deg; Schutz 2011), for which the observed emission is significantly depressed and effectively undetectable (Abbott et al. 2017b,

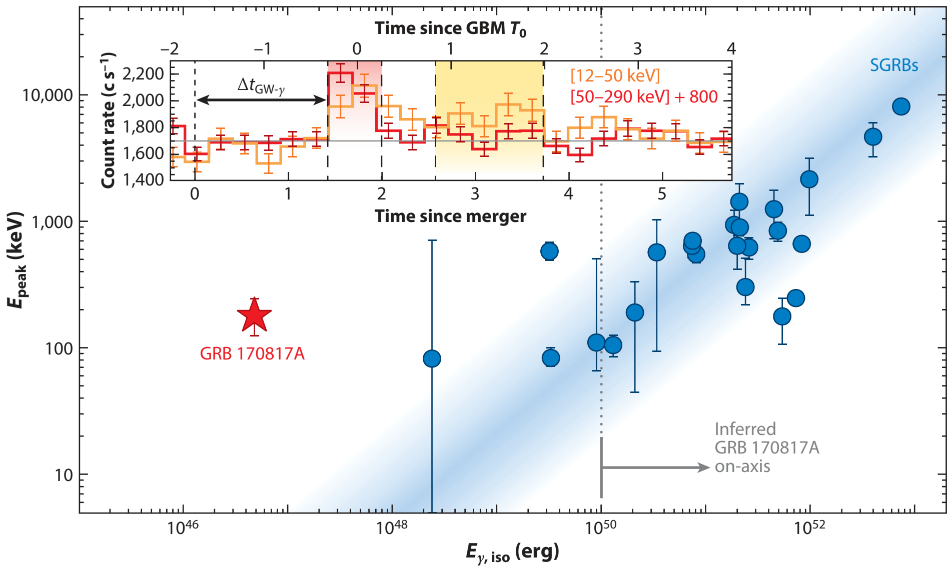

Figure 2

With significantly lower $E_{\gamma,\text{iso}}$ but comparable E_{peak}, the observed properties of GRB 170817A (*red star*) clearly deviate from those of SGRBs (*blue circles*; values from Salafia et al. 2019). (*Inset*) The *Fermi*-GBM light curve of GRB 170817A shows a peculiar morphology, with a short hard main pulse of ∼0.5 s (*red shaded area*) followed by a softer tail of emission with duration of ∼1.12 s (*yellow shaded area*). The onset of the γ-ray emission is delayed compared to the merger time of $\Delta t_{\text{GW-}\gamma}$. Abbreviations: GBM, γ-ray burst monitor; SGRBs, short γ-ray bursts.

Goldstein et al. 2017) at the typical distances and jet collimation angles of SGRBs ($z \approx 0.5$, $\theta_{\rm jet} \sim$ 4–15 deg; Berger 2014, Fong et al. 2015). The true surprise is that the first GW-detected BNS merger was also accompanied by the independent detection of γ-rays.

Top-hat jet: jet with all the energy uniformly distributed and confined within $\theta \leq \theta_{\rm jet}$

3.1. Relationship to the Gamma-Ray Emission from Short Gamma-Ray Bursts

With $E_{\gamma,\,\rm iso} = (4.8 \pm 0.9) \times 10^{46}$ erg and a peak luminosity $L_{\rm peak,\,iso} = (1.4 \pm 0.5) \times 10^{47}\,{\rm erg\,s^{-1}}$, GRB 170817A is orders of magnitude less energetic and luminous than SGRBs, yet with similar duration of ~2 s. This opens two possibilities: (*a*) GRB 170817A is intrinsically subenergetic and represents a new class of γ-ray transients associated with BNS mergers, or (*b*) GRB 170817A is a normal SGRB viewed off axis. The afterglow observations of Section 5 require an off-axis collimated outflow with large amounts of energy similar to that of cosmological SGRBs, ruling out the first scenario. In the context of an off-axis view of a relativistic top-hat jet, the off-axis correction factor necessary to bring the observed $E_{\gamma,\,\rm iso}$ of GRB 170817A in line with that of SGRBs would lead to an extremely large intrinsic peak energy of $\gtrsim$3 MeV and to a viewing angle fortuitously just outside the jet ($\theta_{\rm obs} - \theta_{\rm jet} \approx 1$ deg), which is inconsistent with the late afterglow turn-on of Section 5 (Abbott et al. 2017b, Granot et al. 2017, Kasliwal et al. 2017b, Murguia-Berthier et al. 2017a). The conclusion is that the observed γ-rays require the presence of a structured outflow with energy $E > 0$ and Lorentz factor $\gamma > 0$ outside the jet core at $\theta > \theta_{\rm jet}$. The off-axis view ultimately enabled us to appreciate the presence of this structure, which has a primary role in shaping the peculiar light-curve morphology of GRB 170817A, and allowed energetically subdominant components (to which the on-axis SGRB phenomenology is largely insensitive) to emerge.

Finally, we consider the energetics of GRB 170817A in the context of the γ-ray luminosity function of SGRBs (Sun et al. 2015, Wanderman & Piran 2015, Ghirlanda et al. 2016). With $L_{\rm peak,\,iso} = (1.4 \pm 0.5) \times 10^{47}\,{\rm erg\,s^{-1}}$, GRB 170817A extends the luminosity function of SGRBs by more than two orders of magnitude and implies a current local rate of $\rho_\gamma (L_{\rm peak,iso} > 10^{47}\ {\rm erg\,s^{-1}}) \geq 190^{+440}_{-160}\, f_{{\rm b}\gamma}^{-1}\ {\rm Gpc^{-3}\ year^{-1}}$ (Zhang et al. 2018), where $f_{{\rm b}\gamma} \equiv [1 - \cos(\theta_\gamma)]$ is the beaming factor and θ_γ is the opening angle of the γ-ray emission. For typical efficiencies of kinetic energy–to–γ-ray emission conversion $\epsilon \approx$ 10–20%, the GW170817 afterglow energetics of Section 5 point to an on-axis value of $L^{\rm on\text{-}axis}_{\rm peak,iso} > 10^{51}\ {\rm erg\,s^{-1}}$ (Nakar & Piran 2018, Ghirlanda et al. 2019, Salafia et al. 2019), for which the current local rate derived from the SGRB luminosity function is $\rho_j (L_{\rm peak,iso} > 10^{51}\ {\rm erg\,s^{-1}}) \approx 0.5\ f_{{\rm b}j}^{-1}\ {\rm Gpc^{-3}\ year^{-1}}$. A comparison of ρ_γ and ρ_j assuming that the SGRB luminosity function maps the properties of SGRB jets seen on axis (at least at the high luminosities of $L_{\rm peak,iso} > 10^{51}\ {\rm erg\,s^{-1}}$ of interest; e.g., Beniamini et al. 2019) and that GW170817 seen on axis belongs to this distribution leads to $f_{{\rm b}\gamma} \gtrsim 380^{+7495}_{-343}\, f_{{\rm b}j}$ or $\theta_\gamma \gtrsim 60\ {\rm deg}^{+30}_{-40}$ for $\theta_{\rm jet} \sim 3$ deg (Section 5). Similarly, by requiring the local rate of events with wide-angle γ-ray emission ρ_γ to be at most the BNS merger rate inferred from GWs ($\mathfrak{R} = 980^{+1490}_{-730}\ {\rm Gpc^{-3}\ year^{-1}}$; Abbott et al. 2020a), $\theta_\gamma \gtrsim 36\ {\rm deg}^{+54}_{-25}$ is inferred, where θ_γ is the collimation angle of the γ-ray emission. As shown by **Figure 3**, current GW and EM observations are thus consistent with the notion that most (if not all) BNS mergers produce jets with typical $\theta_{\rm jet}$ of a few to ten degrees (Beniamini et al. 2019) and that all SGRBs might be accompanied by wider-angle γ-ray emission similar to that of GRB 170817A. Given the low luminosity of this component, it is no surprise that it eluded detection in SGRBs. GRB 170817A-like events would be detectable only out to ~55–80 Mpc with current γ-ray spacecraft (Abbott et al. 2017b, Goldstein et al. 2017, Zhang et al. 2018).

3.2. Origin of Gamma-Rays in This Event

The observed delay between the BNS merger and GRB 170817A ($\Delta t_{\rm GW\text{-}\gamma} = 1.74 \pm 0.05$ s) is a novel multimessenger observational parameter, which we assume is astrophysical in origin (i.e.,

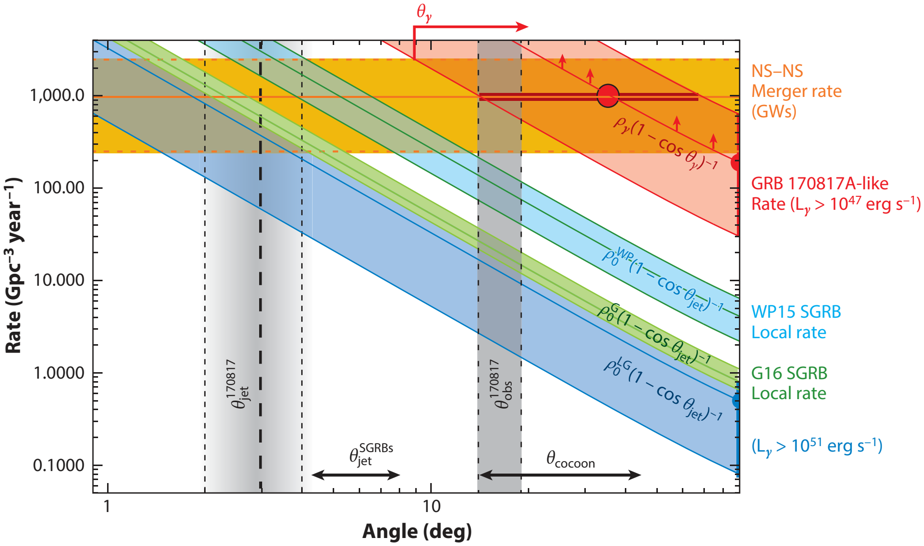

Figure 3

Inferred beaming-corrected local rate of GRB 170817A -like bursts (*red area*; Zhang et al. 2018) and cosmological SGRBs (from Wanderman & Piran 2015 and Ghirlanda et al. 2016; in *light blue* and *green*, respectively) as a function of beaming angle. The local rate of SGRBs with luminosity similar to the inferred on-axis γ-ray luminosity of GW170817 is shown in blue (Ghirlanda et al. 2019). A comparison with the local rate of NS–NS mergers from GW observations (*orange area*; Abbott et al. 2020a) reveals that GRB 170817A likely produced γ-rays detectable from a relatively large $\theta_\gamma > 10$ deg, which is significantly larger than $\theta_{jet} \approx 2$–4 deg (Section 5) and consistent with the inferred observer location $\theta_{obs} \approx 14$–19 deg (Section 5). The range of SGRBs θ_{jet} is indicated by the leftmost black arrow (Section 5). The range of angular extent θ_{cocoon} of cocoon outflows/jet wings is also indicated (e.g., Lazzati et al. 2017b, Gottlieb et al. 2018b, Kathirgamaraju et al. 2019b). Abbreviations: GW, gravitational wave; NS, neutron star; SGRB, short γ-ray burst.

GWs and light propagate at the same speed; see also Section 6.3). $\Delta t_{GW\text{-}\gamma}$ has three major components (Zhang 2019): the jet injection time Δt_{inj}, the jet and/or cocoon breakout time Δt_{bo}, and the time it takes for the emitting material to reach the transparency radius Δt_{tr}, where the γ-rays can freely escape. These quantities are not well known from theory and are not well constrained by observations, yet they represent fundamental aspects of the BNS merger physics. Numerical simulations of SGRB jets breaking through neutrino-driven and magnetically driven winds (Murguia-Berthier et al. 2017b) and dynamical ejecta (Nagakura et al. 2014, Gottlieb et al. 2018a) suggest $\Delta t_{bo} \approx$ a few 100 ms, with high sensitivity on the properties of the ejecta cloud. Observations of γ-rays from SGRBs suggest similar values of ≈200–500 ms (Moharana & Piran 2017). Δt_{inj} (≈10 ms to seconds) depends on the type of jet launching mechanism and likely reflects the timescale needed to form an accretion disk or strong magnetic fields, as well as the timescale for the HMNS (if one was formed) to collapse to a BH (e.g., Granot et al. 2017). Because the properties of the expanding merger ejecta cloud (i.e., density, radius, and angular distribution) as seen by the jet strongly depend on how delayed the jet injection is, the structure and energy partitioning $E(\Gamma\beta)$ within the outflow that result from the jet interaction with the merger's ejecta are also very sensitive to Δt_{inj} (e.g., Murguia-Berthier et al. 2021).

Compactness arguments applied to the main nonthermal pulse of GRB 170817A set a limit on the wide-angle outflow Lorentz factor $\Gamma \gtrsim 2.5$ for the source to be optically thin to

e^+e^- pair production, which, together with the observed pulse duration, implies a radius of emission $R_\gamma = 2c\Gamma^2\delta t_{\rm obs} \gtrsim 10^{11}$ cm (Kasliwal et al. 2017b, Gottlieb et al. 2018b, Matsumoto et al. 2019). There are two main potential physical scenarios to explain GRB 170817A. GRB 170817A might have been produced by some dissipative process within less-energetic wide-angle jet wings around the ultrarelativistic jet core (e.g., Lazzati et al. 2017b, Meng et al. 2018, Geng et al. 2019, Ioka & Nakamura 2019, Kathirgamaraju et al. 2019b) or by shock breakout emission of the cocoon (inflated by the jet) as it emerged from the merger ejecta (Section 1.4; Bromberg et al. 2018, Gottlieb et al. 2018b, Nakar et al. 2018). Both scenarios involve the presence of a mildly relativistic, laterally extended outflow component, yet with some key differences discussed below. We note that these two scenarios are not mutually exclusive: The cocoon shock breakout emission is a robust phenomenon for both hydrodynamic and magnetic jets, with magnetic jets being able to develop structure even after breakout as a consequence of the propagation of a rarefaction wave (Bromberg et al. 2018, Geng et al. 2019, Kathirgamaraju et al. 2019b).

The cocoon shock breakout scenario requires R_γ to coincide with the breakout radius $R_{\rm bo}$ from the merger ejecta, which in turn requires the existence of a fast tail of merger ejecta with $v \sim 0.6$–$0.8c$ (which is much faster than the bulk of the ejecta; Section 4) that is able to reach R_γ at $\Delta t_{\rm GW-\gamma}$ (Bromberg et al. 2018, Gottlieb et al. 2018b). Interestingly, BNS simulations have suggested the presence of such a fast tail of dynamical ejecta with $v \gtrsim 0.6c$ and mass up to $\sim 10^{-5}\ {\rm M_\odot}$ originating from the interface of the merging NSs (e.g., Bauswein et al. 2013; Hotokezaka et al. 2013, 2018; Kyutoku et al. 2014). In the jet-wings scenario, R_γ has instead no knowledge of the fastest merger ejecta tail and it is not bound to within their location at $\Delta t_{\rm GW-\gamma}$.

An interesting implication is that in the cocoon shock breakout scenario, the angular timescale $\sim R_\gamma/(2c\Gamma^2)$ can be too short to account for $\Delta t_{\rm GW-\gamma}$, and $\Delta t_{\rm inj}$ has to contribute a sizeable fraction of the observed delay [e.g., Gottlieb et al. (2018b), Nakar et al. (2018) and Bromberg et al. (2018) assume $\Delta t_{\rm inj} = 0.8$ s and 0.5 s, respectively]. In this framework, the observed $\Delta t_{\rm GW-\gamma} \approx T_{90}$ is mostly a chance coincidence. Jet-wings scenarios can instead invoke larger angular timescales of $\sim$2 s that regulate both the delay and the duration of the GRB (Zhang et al. 2018, Geng et al. 2019, Zhang 2019): The observed $\Delta t_{\rm GW-\gamma} \approx T_{90}$ can thus be interpreted as a natural consequence of $\Delta t_{\rm GW-\gamma}$ being dominated by the time necessary for the jet to travel to the transparency radius, with a negligible jet launching time ($\Delta t_{\rm inj} < \Delta t_{\rm GW-\gamma}$). A similar situation can also happen within cocoon shock breakout scenarios, if the jet energy is near the critical minimum value for jet breakout, which leads to a small difference between the shock velocity and the homologous ejecta velocity and, hence, a delayed breakout time on timescales longer than the engine duration (i.e., $\Delta t_{\rm bo} \approx \Delta t_{\rm GW-\gamma}$; late breakout scenario of Duffell et al. 2018). Finally, in the cocoon shock breakout scenario, the peculiar light-curve morphology of GRB 170817A and its hard-to-soft spectral evolution naturally result from the transition of the cocoon shock hydrodynamics from a planar to a spherical phase (Gottlieb et al. 2018b). In jet-wings models the spectral softening might be related to the jet structure and/or the emergence of thermal components (Meng et al. 2018).

To conclude, though it is difficult to rule out either set of models with high confidence based on the γ-rays from this single event, there are predictions that link $\Delta t_{\rm GW-\gamma}$, M_{ej}, and the relative energy radiated by the γ-ray pulse and the total afterglow kinetic energy that can be tested with a statistical sample of NS–NS (and NS–BH) mergers.

4. AT 2017gfo: UV–OPTICAL–IR THERMAL EMISSION

A worldwide effort commenced after the discovery of AT 2017gfo to obtain UV, optical, and NIR photometry from many telescopes (Andreoni et al. 2017, Arcavi et al. 2017, Coulter et al. 2017, Cowperthwaite et al. 2017, Díaz et al. 2017, Drout et al. 2017, Evans et al. 2017, Hu et al. 2017,

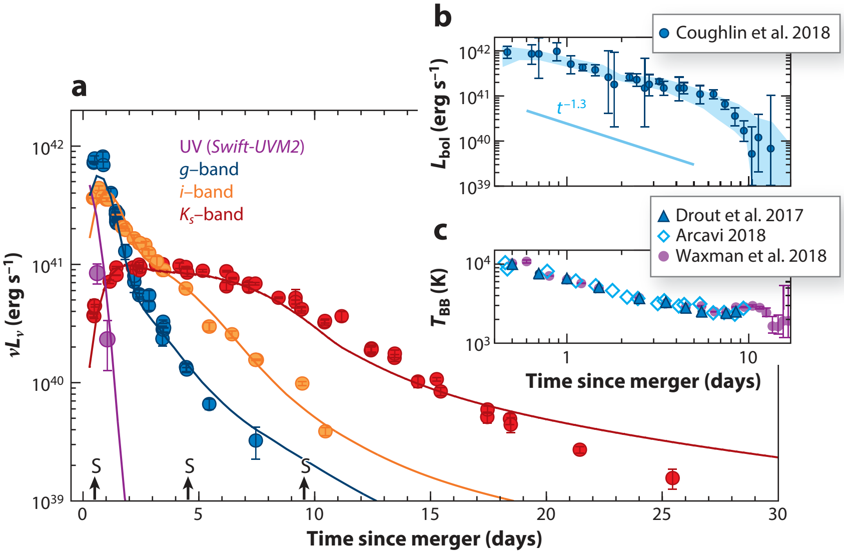

Figure 4

(*a*) Light curves of AT 2017gfo in four representative filters: UV from *Swift-UVM2* ($\lambda_{\rm eff} = 2231$ Å), *g* ($\lambda_{\rm eff} = 4671$ Å), *i* ($\lambda_{\rm eff} = 7458$ Å), and K_s ($\lambda_{\rm eff} = 2.14$ μm). Data and best-fitting three-component model from Villar et al. (2017), with original data presented in the references cited in Section 4. Vertical arrows indicate the times of the spectra displayed in **Figure 5**. (*b*) Bolometric luminosity from Coughlin et al. (2018) (*blue circles* with uncertainties). The shaded blue area marks the range of best-fitting bolometric light curves from the literature (Cowperthwaite et al. 2017, Drout et al. 2017, Arcavi 2018, Waxman et al. 2018). The solid blue line shows a slope of $L_{\rm bol} \propto t^{-1.3}$, which is the expected slope of energy input from *r*-process radioactive decay. (*c*) Best-fitting blackbody temperatures $T_{\rm BB}$ (Drout et al. 2017, Arcavi 2018, Waxman et al. 2018). Note that Drout et al. (2017) fixed $T_{\rm BB} = 2{,}500$ K after $\delta t = 8.5$ days.

Kasliwal et al. 2017b, Lipunov et al. 2017, Pian et al. 2017, Shappee et al. 2017, Smartt et al. 2017, Soares-Santos et al. 2017, Tanvir et al. 2017, Troja et al. 2017, Utsumi et al. 2017, Valenti et al. 2017, Pozanenko et al. 2018). The combined data set on AT 2017gfo contains more than 600 individual data points from 46 instruments [as compiled by Villar et al. (2017)]. The light curves of AT 2017gfo are displayed in **Figure 4**, and a few representative spectra are shown in **Figure 5**.

For clarity, in **Figure 4** we select four representative filters with high temporal sampling to demonstrate the photometric behavior of AT 2017gfo from the near-UV (*Swift-UVM2*), blue optical (*g*), and red optical (*i*), and through the NIR (K_s). The UV light curves exhibit fading behavior from the first observations at $\delta t = 0.65$ days (Evans et al. 2017). At the other extreme, the K_s light curve rose to a broad peak around $\delta t \approx 3.5$ days. In between these extremes, the optical emission started fading within a day after the merger (Arcavi et al. 2017, Coulter et al. 2017, Cowperthwaite et al. 2017, Kasliwal et al. 2017b, Pian et al. 2017, Smartt et al. 2017, Soares-Santos et al. 2017).

Optical spectroscopy in the first week after the merger was presented by a number of groups (Andreoni et al. 2017, Kasliwal et al. 2017b, Levan et al. 2017, McCully et al. 2017, Nicholl et al. 2017, Pian et al. 2017, Shappee et al. 2017, Smartt et al. 2017, Troja et al. 2017, Valenti et al. 2017), with the first spectrum acquired at $\delta t = 0.5$ days after merger. The spectra were unlike those of known SNe and only developed weak features before the transient became too faint at $\delta t \approx 10$ days. NIR spectroscopy was obtained from a few sources starting at $\delta t = 1.5$ days (Chornock et al. 2017, Kasliwal et al. 2017b, Pian et al. 2017, Smartt et al. 2017, Tanvir et al. 2017, Troja et al. 2017), and resulted in the detection of a number of broad features in the range of 1–2 μm.

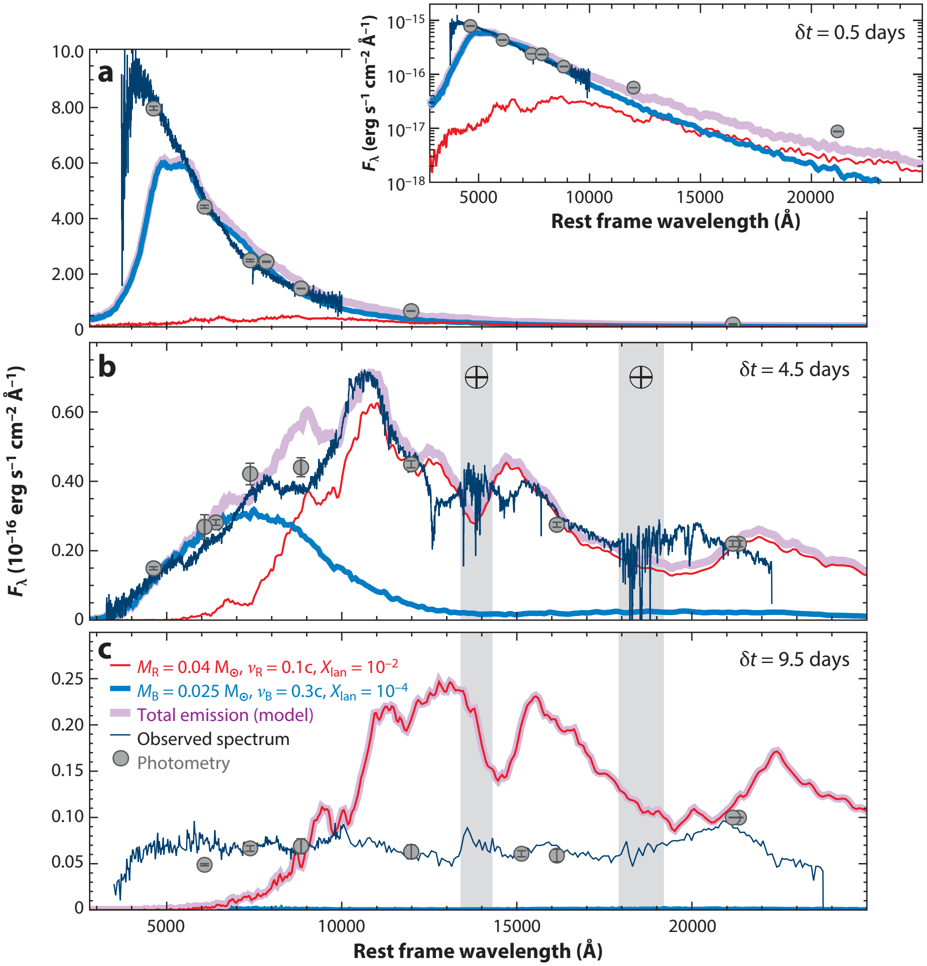

Figure 5

Spectral evolution of AT 2017gfo compared with two-component kilonova models from Kasen et al. (2017). Each panel [$\delta t = 0.5$ days (*a*), 4.5 days (*b*), and 9.5 days (*c*) after merger] shows a selected spectrum in navy blue (data from Pian et al. 2017, Shappee et al. 2017, and Smartt et al. 2017), a low-lanthanide KN model (*blue*), a high-lanthanide KN model (*red*), and their sum (*purple*). The KN models have the properties listed in the legend. Gray circles show the photometry interpolated from the compilation by Villar et al. (2017). *Inset:* Same data and models as those in the main panel at $\delta t = 0.5$ days, but with a logarithmic flux scale to better show the NIR excess over the pure low-lanthanide blue KN model even at early times. Gray bands mark the regions most affected by telluric absorption. Abbreviations: KN, kilonova; NIR, near-infrared.

We display three epochs of spectroscopy in **Figure 5** to sample the evolution of the spectral energy distribution (SED). The first epoch ($\delta t = 0.5$ days) is dominated by a blue component of emission (Shappee et al. 2017), whereas the second epoch ($\delta t = 4.5$ days) was chosen to demonstrate the epoch with the clearest broad features in the NIR (Chornock et al. 2017, Pian et al. 2017, Smartt et al. 2017). The final epoch ($\delta t = 9.5$ days) shows the persistence of some of those NIR features even as the transient became difficult to observe and the signal-to-noise ratio became poor.

4.1. Basic Properties and Relationship to Other Optical Transients

Here, we summarize the most important phenomenological features of AT 2017gfo:

- **Peak bolometric luminosity of ~10^{42} erg s^{-1}:** This is comparable with the peak luminosities of some core-collapse SNe and is substantially greater than some of the prior predictions from kilonova models incorporating lanthanide opacities.
- **Thermal SED at early times:** The SED (spectral energy distribution) is reasonably well characterized by a blackbody function at the earliest epochs for which we have data. In particular, the first UV data at $\delta t = 0.6$ days result in an SED that has too much curvature to be well fitted by a power-law function, which is inconsistent with the synchrotron spectra of GRB afterglows (e.g., Evans et al. 2017). Deviations from a blackbody SED grew over time.
- **Fast fading in the optical:** In the seven days after the first optical detection, the transient faded by 3.90 ± 0.18 mag in *i* and 5.87 ± 0.34 mag in *g* (**Figure 4**; Cowperthwaite et al. 2017, Drout et al. 2017, Siebert et al. 2017, Villar et al. 2017).
- **Large expansion velocities of the optical photosphere:** Shappee et al. (2017) analyzed the first spectrum of AT 2017gfo (**Figure 5**) and found a color temperature of $T_{\rm BB}$=$11{,}000^{+3{,}400}_{-900}$ K (90% c.l.). Given the luminosity of the source, the material at the photosphere had to be ejected at a velocity of $0.26^{+0.02}_{-0.07}c$ to reach the large implied photospheric radius ($3.3^{+0.3}_{-0.8} \times 10^{14}$ cm) in the $\delta t = 0.50$ days after the merger. Similar analyses based on blackbody radii inferred from either spectra or photometry require expansion velocities to be around 0.3c during the first day and remain above 0.1c for the first ~7 days after the merger (Cowperthwaite et al. 2017, Drout et al. 2017, Evans et al. 2017, Kasliwal et al. 2017b, Nicholl et al. 2017, Pian et al. 2017, Troja et al. 2017).
- **Rapid cooling of the photospheric temperature:** Cooling is apparent in the photometry even within 1 day of the merger (**Figure 4**). The peak of the SED moved out of the optical and longward of 1 μm by $\delta t \approx 5$ days. After ~8 days, the color temperature of the ejecta ($T_{\rm BB}$) asymptotically approached ~2,500 K, which is a very unusual value.
- **Lack of SN-like features in optical spectra:** The initial optical spectra were smooth and blue, with a peak near ~4000 Å (Shappee et al. 2017). Over the next few days, the spectra developed a peak that rapidly moved red toward the NIR, but never exhibited the clear P-Cygni features found in SNe (Kilpatrick et al. 2017, McCully et al. 2017, Nicholl et al. 2017, Pian et al. 2017, Shappee et al. 2017, Smartt et al. 2017). Instead, a few broader features ($\Delta\lambda/\lambda \approx 0.1$–$0.2$) developed at red optical wavelengths (minima near 7400 and 8300 Å) and in the NIR (**Figure 5**; Chornock et al. 2017, Pian et al. 2017, Smartt et al. 2017, Tanvir et al. 2017, Troja et al. 2017). The severe blending of spectral features was interpreted as requiring high expansion velocities of 0.2–0.3c for the material emitting in the optical and ~0.1c for the material that dominated the NIR emission.

This combination of properties is unprecedented for an optical transient. No previously known SN light curve fades as rapidly as AT 2017gfo (e.g., Arcavi et al. 2017, Siebert et al. 2017, Smartt et al. 2017). The spectra do not resemble those of known classes of transients. Two separate arguments, line blending and the required expansion velocities of the inferred blackbody radii, lead to the conclusion that the material dominating the optical emission in the first few days expanded at velocities of roughly 30% the speed of light, which is high even for an SN.

Particular focus is due the unusually red colors of AT 2017gfo after the first week ($g - K_s \gtrsim 5$ mag; $T_{\rm BB} \approx 2{,}500$ K). This is an extraordinary SED for an astronomical transient. By contrast, the hydrogen-rich atmospheres of Type II SNe asymptotically approach color temperatures around 5,000 K on the photometric plateau due to the jump in opacity provided by hydrogen recombination near this temperature. The emission from the iron-rich ejecta of Type Ia SNe is not well described by a blackbody spectrum, but the color temperatures are also near 6,000 K due to the wavelength dependence of the opacity of iron-peak elements. This immediately implies that the ejecta of AT 2017gfo must have sources of opacity (and, presumably, a composition) unlike those found in normal SNe. Gall et al. (2017) demonstrate that dust formation does not provide a plausible alternative interpretation. Notably, Kasen et al. (2013) predicted that the recombination of Nd and other lanthanide elements would occur at temperatures near 2,500 K, providing a natural explanation for a kilonova to have a photospheric temperature regulated to around this value.

4.2. Kilonova Models

The light curves of astronomical transients powered by diffusion of energy deposited by radioactive decay rise to a peak that occurs when the diffusion timescale through the ejecta is comparable to the time after explosion (Arnett 1982). The luminosity near the peak is roughly equal to the instantaneous rate of energy deposition for many reasonable models. In the case of an r-process-powered kilonova, Metzger (2019) provides these relationships:

$$\begin{aligned} t_{\rm peak} &\approx 1.6\ {\rm days} \left(\frac{M}{10^{-2}\ {\rm M}_\odot}\right)^{1/2} \left(\frac{v}{0.1c}\right)^{-1/2} \left(\frac{\kappa}{1\ {\rm cm}^2\ {\rm g}^{-1}}\right)^{1/2}, \\ L_{\rm peak} &\approx 10^{41}\ {\rm erg\,s}^{-1} \left(\frac{\epsilon_{\rm th}}{0.5}\right) \left(\frac{M}{10^{-2}\ {\rm M}_\odot}\right)^{0.35} \left(\frac{v}{0.1c}\right)^{0.65} \left(\frac{\kappa}{1\ {\rm cm}^2\ {\rm g}^{-1}}\right)^{-0.65}, \end{aligned} \qquad 1.$$

where M is the mass of the ejecta, v is the scale velocity of the ejecta, $\epsilon_{\rm th}$ is a parameter describing the thermalization efficiency of input radioactive heating, and κ is a gray opacity. It can immediately be seen that the high peak luminosity of AT 2017gfo and short optical risetime are incompatible with high opacities. A similar analysis led Drout et al. (2017) to conclude that the emitting material in the first 0.5 days is constrained to have an opacity of $\kappa < 0.08\ {\rm cm}^2\ {\rm g}^{-1}$.

There are a number of important simplifying assumptions underlying these expressions, especially that κ is constant throughout the ejecta, even over time as the ejecta cool and recombine. The energy input originates from a superposition of numerous radioactive isotopes, whose half-lives are distributed approximately uniformly in time, which results in a power-law heating rate (Li & Paczyński 1998). Detailed studies have found that the overall heating rate is $\propto t^{-1.3}$, which we show as the blue line in **Figure 4*b*** (Metzger et al. 2010, Barnes et al. 2016), although the normalization depends on the assumed nuclear mass model (e.g., Rosswog et al. 2017). Another key ingredient is the thermalization efficiency, which is expected to decrease over time (e.g., Kasen & Barnes 2019, Hotokezaka & Nakar 2020). However, by assuming $\epsilon_{\rm th} \approx 0.5$ at early times and taking an estimate of the expansion velocities from spectroscopy, the model reduces to a pair of equations to solve for the required opacities and ejecta masses to produce the observed timescales and luminosities.

Diffusion-powered light curve models can be fit to the bolometric light curve of a transient by specifying a gray opacity motivated by the expected composition. With a prescription for the color temperature (e.g., from blackbody considerations), the fits can be performed on individual filters. These Arnett-like light curve models with only a single component of emission do not fit AT 2017gfo very well because of the difference in timescales between the blue and NIR light curves. Instead, the range of outflow properties seen in numerical simulations of BNS mergers motivates exploration of multicomponent models. Then one component with a small diffusion timescale can dominate in the bluest filters and at the earliest times, whereas a longer timescale component can supplement the emission at later times and in the NIR (Cowperthwaite et al. 2017, Drout et al. 2017, Kilpatrick et al. 2017). As an example, the best-fit three-component model from Villar et al. (2017) is shown in **Figure 4**.

To move beyond Arnett-like models requires sophisticated radiative transfer modeling based on the latest atomic data. The quantitative set of inferences about composition and ejecta masses for AT 2017gfo in the initial observational papers in 2017 were primarily based on comparisons with only three sets of underlying radiative transfer calculations (Kasen et al. 2017, Tanaka et al. 2018, Wollaeger et al. 2018). One important distinction is that Kasen et al. (2017) and Tanaka et al. (2018) use an expansion opacity formalism to treat the millions of bound–bound line transitions (Karp et al. 1977, Eastman & Pinto 1993), whereas the models of Wollaeger et al. (2018) instead used a line-smeared approach to opacities (Fontes et al. 2017), which tends to result in even higher lanthanide opacity. Subsequent to GW170817, all groups have continued to refine the underlying atomic physics and numerical techniques (e.g., Kasen & Barnes 2019, Fontes et al. 2020, Tanaka et al. 2020).

Another fundamental difference in the approaches taken by these models is that both Tanaka et al. (2018) and Wollaeger et al. (2018) anchor their models to ejecta properties and composition distributions (Y_e) from numerical simulations of nucleosynthesis in BNS merger ejecta, including both dynamical ejecta and winds (Perego et al. 2014, Rosswog et al. 2014, Wanajo et al. 2014). The models of Kasen et al. (2017) have only three free parameters, a total mass of the ejecta, an average velocity (defined as $v = \sqrt{2E_k/M}$ with E_k the kinetic energy), and a fractional lanthanide concentration X_{lan}. Because the open *f*-shell lanthanides dominate the opacity whenever they are present, X_{lan} captures the most important parameter of the underlying nucleosynthesis for affecting the kilonova SED. Tanaka et al. (2020) connect X_{lan} and κ to different Y_e ranges seen in their radiative transfer models under typical kilonova conditions. The highest opacities ($\kappa \approx 20$–$30\ \mathrm{cm^2\ g^{-1}}$) and lanthanide abundances ($X_{lan} \approx 0.1$–0.2) are provided by material with $Y_e < 0.2$. Conversely, material with $Y_e \approx 0.4$ has essentially zero lanthanide production, and yet still has an opacity of $\kappa \approx 1\ \mathrm{cm^2\ g^{-1}}$ due to the light *r*-process elements. Ejecta with intermediate lanthanide abundances ($X_{lan} \approx 10^{-3}$–10^{-2}) are produced in a narrow range of Y_e near 0.25, and have opacities of $\kappa \approx 5\ \mathrm{cm^2\ g^{-1}}$.

In **Figure 5*a***, we compare a low-lanthanide blue kilonova model to the earliest spectrum of AT 2017gfo (Kasen et al. 2017, Kilpatrick et al. 2017, Shappee et al. 2017). The velocity parameter was chosen to be $0.3c$ to match the inferred expansion velocity of the optical photosphere, and X_{lan} was constrained to be below $\sim 10^{-4}$ to match the optical/NIR flux ratio. The mass of $0.025\ M_\odot$ is then necessary to match the flux level. By the epoch of **Figure 5*b*** ($\delta t = 4.5$ days), the blue kilonova had faded and cooled. The prominent NIR features are a good match for a red kilonova model with mass $0.04\ M_\odot$, $v = 0.1c$, and a higher lanthanide abundance of $X_{lan} = 0.01$ (Chornock et al. 2017). Kasen et al. (2017) identify Nd as the likely dominant source of these features. Taking the same kilonova models and extrapolating them forward to $\delta t = 9.5$ days results in the poor fit in **Figure 5*c***. The models overproduce the flux at this epoch, which can be somewhat alleviated by reducing the overall mass in each component, at the expense of a worse match at early times. At this late time, the radiative transfer or thermalization assumptions may be violated as the ejecta transition to being optically thin.

Fits using the models of Wollaeger et al. (2018) find that the early emission from AT 2017gfo can be reproduced using a relatively massive (0.01–0.03 $M_\odot$) and moderately neutron-rich ($Y_e \approx 0.27$) postmerger wind component, with a subdominant neutron-rich dynamical ejecta component necessary to produce NIR emission on longer timescales (Evans et al. 2017, Tanvir et al. 2017, Troja et al. 2017). Tanaka et al. (2017) found that 0.03 $M_\odot$ of material with a broad range of compositions ($Y_e = 0.1$–0.4) would underproduce the early blue emission. Adding an ejecta component with moderate Y_e to improve the early light curve increases the total required ejecta mass to $\sim$0.05 $M_\odot$ (Pian et al. 2017).

One caveat to this discussion has to do with the interpretation of $X_{\rm lan}$. Detailed nucleosynthesis calculations of NS merger ejecta find that the production of lanthanides is robust once a strong *r*-process proceeds (e.g., Korobkin et al. 2012, Wanajo et al. 2014). The parameter study by Lippuner & Roberts (2015) finds some dependence of the final lanthanide abundance on the initial entropy and expansion timescale of a merger ejecta parcel, but the primary determinant is Y_e. If it is below a threshold value of $Y_e \approx 0.25$, nucleosynthesis proceeds to the third peak of *r*-process abundances, and $X_{\rm lan} \approx 0.1$. For Y_e somewhat above this threshold, the lanthanide abundance is negligible. Intermediate values require unrealistically narrow ranges of Y_e or macroscopic mixing of high and low lanthanide abundance material to produce an effective $X_{\rm lan}$ in the observed range.

4.3. Evidence for *r*-Process

A very elementary observation supporting the presence of *r*-process nucleosynthesis in AT 2017gfo is that there was an optical–NIR transient to be seen at all, particularly after the first day. The inferred blackbody radii at $\delta t \approx 0.5$ days were $\sim 4 \times 10^{14}$ cm and grew beyond 10^{15} cm in the subsequent days, whereas the merger ejecta were launched from within a few NS radii of the remnant. In the absence of a long-lived source of heating, the ejecta would rapidly lose their internal energy by expanding many orders of magnitude in scale. Even in cocoon models, the inferred radioactive heating of the transient dominates the luminosity after the first day because the cocoon also cools (Kasliwal et al. 2017b, Duffell et al. 2018, Gottlieb et al. 2018a). Other models for the early blue emission discussed below are also applicable only at the earliest times. Normal SNe material is heated by ^{56}Ni, but fits of toy models powered by nickel decay would require $\sim$75% of the ejecta to be composed of radioactive nickel (e.g., Cowperthwaite et al. 2017), which is in contradiction with the observed SED and spectral features. The radioactive species formed as by-products of *r*-process nucleosynthesis provide natural matches to the luminosity and timescale needed to explain AT 2017gfo, particularly for the long-lived NIR component, and any alternative model must provide solutions to these questions.

The fits to the data in the previous section using several models with different assumptions all imply that GW170817 resulted in the ejection of $\sim$0.05 $M_\odot$ of *r*-process material. This needs to be combined with the BNS merger rate to determine whether it matches the required *r*-process production rate to explain Galactic nucleosynthesis, as estimated from the observed abundances of elements such as Eu. Hotokezaka et al. (2015) have estimated that if a class of sources synthesizes 10^{-2} $M_\odot$ of heavy *r*-process (atomic mass $A > 90$) material, the required event rate (averaged over the star-formation history of the Galaxy) is only $\sim$50 Myr^{-1}. This can be compared with the estimated current rate for BNS mergers in the Galaxy of $\mathfrak{R}_{\rm BNS} = 37^{+24}_{-11}$ Myr^{-1} (90% c.l.; Pol et al. 2020), although note that the merger rate is believed to have been higher in the past. Alternatively, the GW-derived BNS rate of $\mathfrak{R} = 980^{+1,490}_{-730}$ Gpc^{-3} year^{-1} (Abbott et al. 2020a) and the density of massive galaxies of $\sim$0.01 Mpc^{-3} can be combined to estimate an average rate of BNS mergers of $\sim$100 Myr^{-1} for typical massive galaxies, which would require ejection of $\sim$0.005 $M_\odot$ of heavy *r*-process material per event. In either case, there is easily sufficient production of *r*-process material in GW170817, assuming that it is typical of BNS mergers, and it is even a little bit high relative to expectations (e.g., Rosswog et al. 2018). Ultimately, moving beyond these order-of-magnitude estimates toward a better understanding of the role of BNS mergers in Galactic nucleosynthesis will require comparison of the detailed measured abundance patterns of stars (e.g., Holmbeck et al. 2020) with numerical simulations of Galactic formation that resolve gas dynamics (e.g., Shen et al. 2015, van de Voort et al. 2015), as well as the accretion of disrupted satellite galaxies (e.g., Roederer et al. 2018).

The resolution of this 60-year-old mystery is a strong claim to make without having provided a confident identification of any particular spectral feature. Instead, the claim is based on the unusual features of the SED ($T_{\rm BB} \approx 2{,}500$ K) and broad spectral features, which reflect theoretical predictions for the unique opacity of material enriched in lanthanides. We also did not present evidence to constrain the detailed abundance pattern beyond estimates of $X_{\rm lan}$. However, the universality of the solar *r*-process abundance pattern in metal-poor stars (Sneden et al. 2008) gives us confidence that if lanthanides have been synthesized, then the other heavy *r*-process elements must be present as well at nearly the standard ratios, which is consistent with the predictions of a wide Y_e distribution in BNS merger ejecta (Korobkin et al. 2012, Bauswein et al. 2013, Rosswog et al. 2014, Wanajo et al. 2014). The unusual spectra at early times are also consistent with predictions for material composed of the light *r*-process (Banerjee et al. 2020).

The primary reason for this somewhat indirect approach (beyond line blending at these ejecta velocities) is that the radiative transfer models described in the previous section are based on atomic structure calculations that still have significant uncertainties. The resulting line lists of bound–bound transitions thus lack the accuracy necessary to be confident of the precise wavelengths of individual transitions. An alternative modeling philosophy is to start with highly accurate, but incomplete, line lists and try to identify a few of the strongest features. This approach was used by Watson et al. (2019), who found that a few very broad lines ($\sim$0.2*c*) of Sr II could match the strongest deviations from a blackbody in the optical spectrum of AT 2017gfo over the first few days after the merger.

The multicomponent kilonova ejecta picture has also been challenged by Waxman et al. (2018), who find a good fit to the bolometric light curve with a single low-opacity component corresponding to $X_{\rm lan} \approx 10^{-3}$, which would be insufficient production to account for the Solar System *r*-process abundances. This is similar to the low-opacity and $Y_e = 0.25$ models of Smartt et al. (2017) and Tanaka et al. (2017), respectively. We note that this does require fine-tuning of the ejecta Y_e because of the strong dependence of lanthanide production on this parameter (Lippuner & Roberts 2015). An alternative is that there is sufficient macroscopic mixing of the ejecta from two components with very different lanthanide abundances as to approximate the overall opacity of a single intermediate component. Actinide abundances in *r*-process-enhanced metal-poor stars may also point to the requirement that material with the lowest Y_e from the dynamical ejecta be mixed with other ejecta components with higher Y_e (Holmbeck et al. 2019). Ji et al. (2019) have also questioned whether GW170817 produced sufficient heavy *r*-process material to account for abundance ratios in metal-poor stars. It is thus important to consider whether there are any other lines of evidence that constrain the presence of the heaviest *r*-process isotopes in the merger ejecta (Section 4.3.1).

4.3.1. Late-time infrared observations. By early September 2017, ground-based optical observations of AT 2017gfo became increasingly difficult due to its rapid fading into the bright background of its host galaxy and then impossible after it entered solar conjunction. Subsequent epochs of optical–IR photometry were obtained with the *Hubble Space Telescope* (HST) and the *Spitzer Space Telescope*. The HST observations only detected the late-time afterglow emission and are discussed in Section 5. *Spitzer* was able to obtain two epochs of 3.6 and 4.5 μm photometry at +43 and +74 days after the merger (Villar et al. 2018, Kasliwal et al. 2019). AT 2017gfo is detected in both epochs at 4.5 μm but not 3.6 μm. The fluxes at 4.5 μm are significantly brighter than the inferred afterglow contribution at that wavelength and thus represent the latest detections of AT 2017gfo. Kasliwal et al. (2019) found that the steep decay between the two *Spitzer* epochs was indicative of a small number of heavy isotopes with half-lives around 14 days powering the radioactive transient. Potentially, this represents our best evidence for the production of second and third peaks of r-process elements in the merger ejecta. Observations of future kilonovae with the *James Webb Space Telescope* (JWST) might directly detect the signatures of these heavy elements (Zhu et al. 2018, Wu et al. 2019).

4.4. Early Blue Emission

One of the most unanticipated results from AT 2017gfo was the luminosity of the early blue emission. The short risetime also places severe constraints on the opacity of the emitting material (Section 4.2). The representative blue kilonova model shown in **Figure 5*a*** matches the luminosity at that epoch, but it experiences too much line blanketing in the blue and underproduces the IR emission (which is remedied by the contribution from the red component). One of the major uncertainties for modeling kilonovae at these early times comes from the paucity of appropriate atomic data for the unusual ejecta conditions. Banerjee et al. (2020) have recently produced opacity calculations for the relevant highly ionized heavy elements and find that they can approximately reproduce the early light curve of AT 2017gfo with $M \approx 0.05\ M_{\odot}$ of lanthanide-poor light r-process material.

The unexpected properties of AT 2017gfo in the first day after the merger have motivated an exploration for alternative models to produce extra blue emission beyond that expected purely from radioactively heated ejecta. Cocoon models produce two effects that can increase the early optical luminosity (Kasliwal et al. 2017b, Gottlieb et al. 2018a). The first is the direct cooling of the jet-deposited energy, which only contributes over the first few hours. The second is the Doppler-boosted emission from the cocoon material, which is moving at mildly relativistic velocities.

Another model was proposed by Piro & Kollmeier (2018), who argued that the asymmetric light curve of AT 2017gfo was not typical of objects whose light curves are governed on both the rise and fall by the same diffusion timescale from a central energy source (e.g., radioactive decay) and instead proposed that merger ejecta surrounding the remnant at larger radius were shock heated and subsequently radiated. However, this picture was challenged by the hydrodynamic simulations of Duffell et al. (2018), who noted the importance of the fact that merger ejecta would be expanding homologously rather than stationary. Their numerical calculations concluded that, for collimated jets with $E_{\mathrm{k}} < 10^{51}$ erg, shock heating due to the jet propagation into the BNS ejecta is energetically subdominant (contributing 10^{48}–10^{49} erg on timescales of 0.1–1 s) and represents a minor contribution to the luminosity of thermal optical transients on longer timescales.

4.5. Relationship to Components in Binary Neutron Star Merger Simulations

We are now in a position to relate the phenomenological components inferred from the optical observations on AT 2017gfo to the various mass-ejection components in BNS merger simulations. The total inferred ejecta mass is too high for only the tidal dynamical ejecta (Sekiguchi et al. 2016), which are also too neutron rich to produce the early optical emission from a lanthanide-poor component (Korobkin et al. 2012). The shock-heated dynamical ejecta can reach sufficiently high velocities to be consistent with the early optical spectra and can be lanthanide poor (Wanajo et al. 2014), but the ejecta masses from this mechanism appear to be too low ($\lesssim 0.01\ M_{\odot}$) unless the NS radius is very small (Oechslin et al. 2007, Bauswein et al. 2013, Hotokezaka et al. 2013). Winds from the accretion disk can produce outflows of a range of compositions, but the velocities may not be sufficiently high to match the early observations (Kasen et al. 2015, Fahlman & Fernández 2018). However, postmerger winds provide the most natural explanation for the high ejecta mass and material being present with a wide range of X_{lan} (Grossman et al. 2014, Metzger & Fernández 2014, Rosswog et al. 2014, Just et al. 2015). The relative importance of winds driven by neutrinos

(Dessart et al. 2009, Metzger & Fernández 2014, Perego et al. 2014), magnetic fields (Metzger et al. 2018), and viscous effects (Radice et al. 2018a) remains an open question.

The numerical simulations of BNS mergers result in highly aspherical ejecta, with high-opacity material commonly being produced in the equatorial plane. The luminosity and SED of the resulting emission are likely to be dependent on the viewing angle, with the general trend being higher luminosities, particularly in the blue, resulting from a more polar viewing angle (e.g., Wollaeger et al. 2018). Despite this effect, many of the studies inferring ejecta parameters from the light curves or spectra of AT 2017gfo have used effectively one-dimensional radiative transfer models. In the case of the multicomponent models discussed in Section 4.2, the flux of the separate components was simply summed to produce the total emission. This can be justified if the ejecta components have separate spatial distributions (e.g., polar versus equatorial) and there is no radiative coupling. However, Kawaguchi et al. (2020) have identified several effects in their two-dimensional models, including photons diffusing preferentially in the directions of low opacity and heating of tidal dynamical ejecta by emission from the postmerger ejecta, that can combine to reduce the inferred total ejecta mass by as much as a factor of about two compared to one-dimensional estimates. There is a clear need for further development of multidimensional radiative transfer models for kilonovae to achieve better precision in estimates of the r-process ejecta mass (Perego et al. 2017; Kawaguchi et al. 2018, 2020; Wollaeger et al. 2018; Korobkin et al. 2021).

4.5.1. Optical polarization. Although the kilonova ejecta are too distant to spatially resolve the various components, the polarization of light can be a useful tool to constrain the geometry. The optical polarization signatures in explosive transients are produced in a competition between the linearly polarizing effects of electron scattering and the depolarizing effects of bound–bound line transitions. If a distant, spatially unresolved source is circularly symmetric when projected on the plane of the sky, the angles of polarization produced locally within the ejecta cancel when integrated over the photosphere. Measurable polarization is thus a signature of deviations from sphericity and has been well studied in the case of SNe (Wang & Wheeler 2008). The highly aspherical geometries of BNS merger ejecta provide a promising avenue to generate polarization.

Covino et al. (2017) were able to obtain five epochs of optical polarimetry of AT 2017gfo, four in R band and one in z. Only the first epoch, at $\delta t = 1.46$ days, had a measurable polarization of $0.50 \pm 0.07\%$, whereas the others had upper limits consistent with this value. Several foreground stars had polarization measurements of similar magnitude and position angle, indicating that most of the observed polarization was produced by propagation through the interstellar medium of the Galaxy. Bulla et al. (2019) concluded that the intrinsic polarization of light from AT 2017gfo itself was $<0.18\%$ at the 95% c.l. Their models showed that future polarimetric observations to probe kilonova ejecta geometry would be most informative at early times, when the low-opacity blue emission is dominant. However, the very high lanthanide line opacities will suppress any polarization signal after emission from the red component dominates the optical light.

4.6. Comparison to Kilonovae in Short Gamma-Ray Bursts

Studies of nearby SGRBs ($z \lesssim 0.5$) have brought to light a significant diversity in the optical emission following SGRBs, which in some cases can be attributed to kilonova emission above the level of the optical afterglow. There are six SGRBs with potential kilonova emission detected, with different levels of observational evidence: SGRBs 050709 (Jin et al. 2016), 060614 (Yang et al. 2015), 070809 (Jin et al. 2020), 130603B (Berger et al. 2013, Tanvir et al. 2013), 150101B (Gompertz et al. 2018, Troja et al. 2018b), and 160821B (Kasliwal et al. 2017a, Lamb et al. 2019b, Troja et al. 2019a). The recently detected SGRB 200522A might provide the first example of a

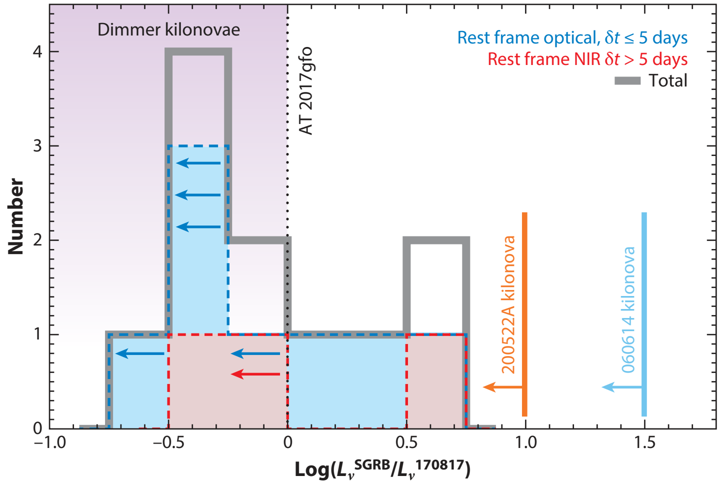

Figure 6

Luminosity distribution of optical counterparts to SGRBs with $z \leq 0.5$ compared with AT 2017gfo, highlighting the diversity of the potential kilonova emission. Only data from bona fide SGRBs for which a kilonova candidate has been identified or SGRBs with brightness limits that are constraining with respect to AT 2017gfo are shown. Rest-frame NIR data (*red*) have been collected at $\delta t > 5$ days with the exception of SGRB 160624A. Optical data (*blue*) have been collected at earlier times ($\delta t \leq 5$ days). Kilonovae in SGRBs like 130603B can be significantly more luminous than AT 2017gfo, whereas existing upper limits rule out an AT 2017gfo-like transient, pointing to the existence of fainter kilonovae or, alternatively, at a class of SGRBs not accompanied by any kilonova emission (e.g., NS–BH mergers would allow that possibility). Optical and NIR limits on kilonovae in SGRBs 060614 and 200522A are shown in light blue and orange, respectively. Data taken from Gompertz et al. (2018), Fong et al. (2020), and Rossi et al. (2020). Abbreviations: BH, black hole; NIR, near-infrared; NS, neutron star; SGRB, short γ-ray burst.

magnetar-boosted kilonova (Fong et al. 2020). In addition, SGRBs 050509B, 061201, 080905A, and 160624A have deep limits that rule out an AT 2017gfo-like kilonova (Gompertz et al. 2018, Ascenzi et al. 2019, Fong et al. 2020, Rossi et al. 2020).

A direct comparison with AT 2017gfo is challenging owing to the very sparse nature of SGRB data (in terms of both spectral and temporal coverage) and a level of contamination by the SGRB afterglow that is difficult to quantify in most cases. The combination of these factors makes it virtually impossible to map the observed diversity of the emission of SGRB kilonova candidates into a constrained physical parameter space of ejecta masses, ejecta velocities, and opacities. The important conclusion is that the current sample of observations of SGRB kilonovae supports the existence of a broad range of kilonova luminosities (≈0.3–10 times the luminosity of AT 2017gfo depending on the epoch and frequency of observation; **Figure 6**). Note that the presence of a successful SGRB oriented toward our line of sight implies that we are viewing these kilonovae from a nearly polar direction, which is believed to be the most luminous viewing angle and least affected by a possible equatorial structure with high opacity. From a population perspective, the complementary (and unsuccessful except for GW170817) search for kilonovae from GW-detected NS mergers also leaves open the possibility that a large fraction of kilonovae from BNS mergers are intrinsically fainter than AT 2017gfo (Kasliwal et al. 2020).

5. GW170817: NONTHERMAL EMISSION

Mass outflows from BNS mergers drive shocks that radiate broadband synchrotron emission. This process converts the shocks' kinetic energy into radiation, with a peak of emission that intrinsically occurs on the outflow's deceleration timescale. For relativistic jets seen off axis, the time of the observed peak of emission further depends on the geometry of the system (i.e., θ_{obs} and θ_{jet}). Two conclusions follow: (*a*) Lighter ejecta components (e.g., relativistic jets; Section 5.1) produce synchrotron emission with an intrinsically earlier peak than that associated with more massive outflows from the merger (e.g., the kilonova ejecta; Section 8.1), and (*b*) synchrotron emission is a probe of both the energy and geometry of the outflows and of the density of matter surrounding the binary at the time of merger (Section 5.1), which is ultimately responsible for the deceleration of the mass outflows.

Following the SGRB literature, we refer to this nonthermal emission as an afterglow. The synchrotron emission depends on the outflow kinetic energy E_k, the environment density n, and the fraction of postshock energy into tangled magnetic fields ϵ_B and accelerated electrons ϵ_e, as well as on the details of the distribution of nonthermal relativistic electrons $N(\gamma_e) \propto \gamma_e^{-p}$ (e.g., Sari et al. 1998). In the case of collimated relativistic outflows, the observed emission carries further dependencies on θ_{jet} and θ_{obs} (**Figure 1**). As of ~3 years after the merger, the nonthermal emission from GW170817 has been dominated by the afterglow of a structured jet seen off axis (Section 5.1; **Figure 7**). Future observations of this very nearby system might reveal the emergence of the first kilonova afterglow (Section 8.1).

5.1. Structure and Geometry of a Jetted Relativistic Outflow

Broadband afterglow observations of GW170817 provide the first direct evidence that BNS mergers are able to launch highly collimated relativistic jets that can survive the interaction with the local merger ejecta, as first theorized by Paczynski (1986) and Eichler et al. (1989), and are likely collimated by this very same process. These observations establish the first direct connection between canonical SGRBs and mergers of NSs, and offer the first view of a SGRB-like relativistic jet from the side (i.e., off axis; see the sidebar titled Jet Terminology).

Key observations include the following: (*a*) deep X-ray and radio nondetections at early times ($t \lesssim 2$ days), which set GW170817 phenomenologically apart from all SGRB afterglows; (*b*) a gradual monotonic rise of the light curve with $F_\nu \propto t^{0.8}$ at $10 \leq \delta t \leq 150$ days (**Figure 7**); (*c*) a sharp achromatic light-curve peak at $\delta t \sim 160$ days; (*d*) steep postpeak decay of $F_\nu \propto t^{-2.2}$ at $\delta t \geq 300$ days; (*e*) a radio-to-X-ray spectrum that is well described at all times by a power-law model of $F_\nu \propto \nu^{-\beta}$ with $\beta \sim 0.583 \pm 0.013$ (**Figure 8**); and (*f*) superluminal motion of the centroid of the unresolved radio image of the blast wave. Below we describe how this combined observational evidence leads to one concordant physical scenario of a highly collimated ($\theta_{jet} \approx 2$–4 deg) ultrarelativistic jet directed away from our line of sight and carrying $\lesssim 10^{51}$ erg that developed wide-angle mildly relativistic ($\Gamma \sim$ few) wings as it propagated through the subrelativistic merger ejecta (i.e., an off-axis structured relativistic jet).

JET TERMINOLOGY

- **Structured jet:** Generic term for an anisotropic outflow with angular and/or radial structure and a core of ultrarelativistic material of angular size θ_{jet}. Structured jets have an angle-dependent bulk Lorentz factor $\Gamma(\theta)$ and an energy per unit solid angle $dE(\theta)/d\Omega$ extending to θ_w with $\theta_w > \theta_{jet}$.
- **Off-axis structured jet:** Structured jet for which $\theta_{obs} > \theta_{jet}$ (not necessarily $\theta_{obs} > \theta_w$).
- **Quasi-spherical outflow:** Uncollimated outflow with potential radial structure and mild angular structure.
- **Cocoon:** Wide-angle mildly relativistic outflow created by the interaction of the relativistic jet with the merger ejecta. A successful jet+cocoon system is a physical manifestation of a structured jet, whereas pure cocoon models belong to the quasi-spherical outflow category.

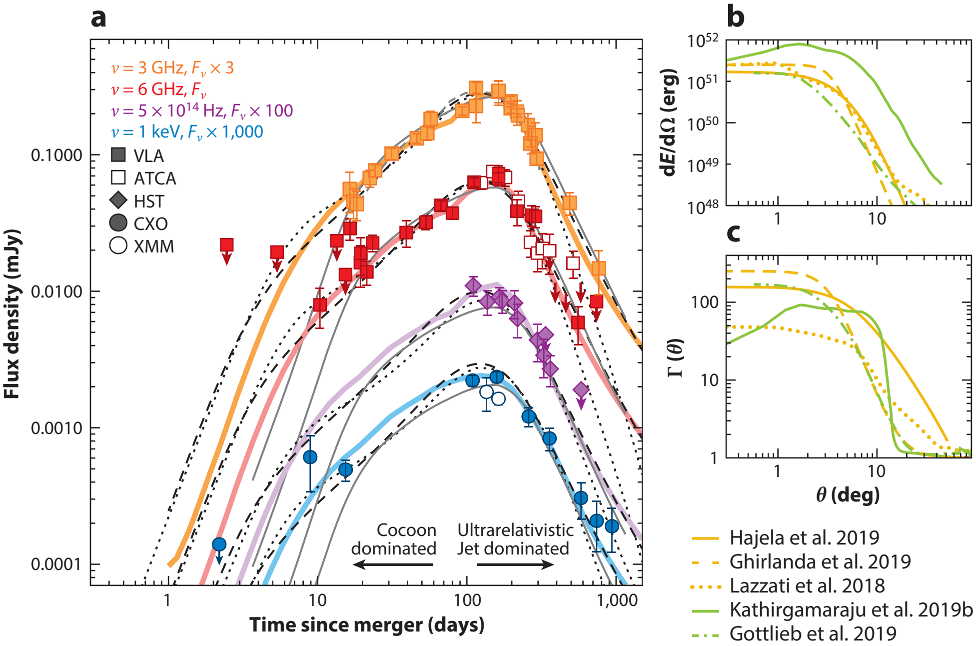

Figure 7

(*a*) Jetted outflows with different angular structures $dE(\theta)/d\Omega$ (*b*) and $\Gamma(\theta)$ (*c*) successfully reproduce the broadband afterglow observations of GW170817 at radio (*orange* and *pink*), optical (*purple*), and X-ray (*blue*) wavelengths. Some models are motivated by the physics of BNS mergers (Lazzati et al. 2018, Gottlieb et al. 2019, Hajela et al. 2019, Kathirgamaraju et al. 2019b), and others are analytical abstractions (e.g., Gaussian jets; Ghirlanda et al. 2019). These models share the presence of a highly collimated core of ultrarelativistic ejecta at $\theta < \theta_{\rm jet}$ viewed off axis ($\theta_{\rm obs} > \theta_{\rm jet}$) and surrounded by mildly relativistic wings of material. Due to relativistic beaming, the prepeak emission is dominated by radiation from the wider-angle mildly relativistic outflow (e.g., a cocoon). The jet core dominated the detected emission at $t \gtrsim t_{\rm peak}$. Observational data originally presented by Alexander et al. (2017, 2018), Haggard et al. (2017), Hallinan et al. (2017), Margutti et al. (2017, 2018), Kim et al. (2017), Troja et al. (2017, 2018a, 2019b, 2020), Dobie et al. (2018), Lyman et al. (2018), D'Avanzo et al. (2018), Mooley et al. (2018a,b), Nynka et al. (2018), Resmi et al. (2018), Ruan et al. (2018), Fong et al. (2019), Hajela et al. (2019), Lamb et al. (2019a), Piro et al. (2019), and Makhathini et al. (2020). Abbreviations: ATCA, Australia Telescope Compact Array; BNS, binary neutron star; CXO, *Chandra X-ray Observatory*; HST, *Hubble Space Telescope*; VLA, Very Large Array; XMM, *X-ray Multi-Mirror Mission-Newton*.

The extremely well-behaved power-law spectrum $F_\nu \propto \nu^{-0.583 \pm 0.013}$ (**Figure 8**) implies that radio and X-ray radiation (and optical as well at $\delta t > 100$ days) are part of the same optically thin synchrotron spectrum, in which the cooling frequency ν_c is above the X-ray band and the synchrotron frequency ν_m is below the radio band at all times. In this regime, $F_\nu \propto \nu^{-(p-1)/2}$, and this leads to the most precise measurement to date of the index p of the relativistic electrons distribution $N(\gamma_e) \propto \gamma_e^{-p}$ accelerated by a BNS merger shock: $p = 2.166 \pm 0.026$ (Fong et al. 2019; see also Hajela et al. 2019, Lamb et al. 2019a, Makhathini et al. 2020, Troja et al. 2020).

Very long baseline interferometry (VLBI) observations provided evidence for an apparent superluminal motion of the radio source centroid with an average velocity $v_{\rm app} = \beta_{\rm app}c = (4.1 \pm 0.5)c$ in the time range of 75–230 days (Mooley et al. 2018a) and constrained the apparent size of the unresolved radio source to <2.5 mas at 270.4 days (90% c.l., Ghirlanda et al. 2019). Taken together

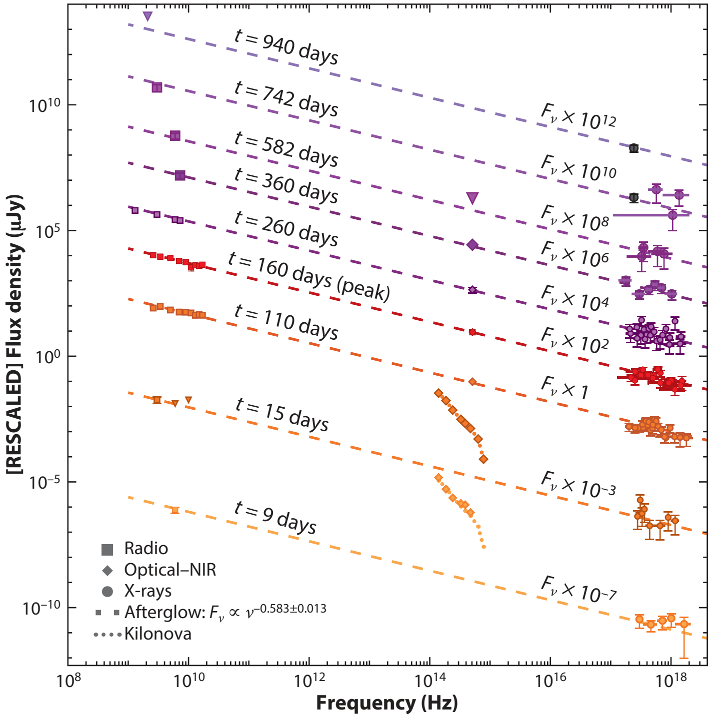

Figure 8

Broadband SED evolution of the jet afterglow of GW170817. X-ray (*circles*) and radio (*squares*) frequencies are dominated by nonthermal synchrotron emission on a simple power-law spectrum $F_\nu \propto \nu^{-\beta_{XR}}$ with $\beta_{XR} = 0.583 \pm 0.013$ at all times (*dashed lines*). During the first weeks the optical bands (*diamonds*) are dominated by thermal kilonova emission (*dotted lines*; Section 4). Black points: 1-keV flux density with flux calibration performed assuming the best-fitting $F_\nu \propto \nu^{-\beta_{XR}}$ spectrum, which is necessary with limited photon statistics. Data taken from Alexander et al. (2017, 2018), Haggard et al. (2017), Hallinan et al. (2017), Margutti et al. (2017, 2018), Kim et al. (2017), Troja et al. (2017, 2018a, 2019b, 2020), Dobie et al. (2018), Lyman et al. (2018), D'Avanzo et al. (2018), Mooley et al. (2018a,b), Nynka et al. (2018), Resmi et al. (2018), Ruan et al. (2018), Fong et al. (2019), Hajela et al. (2019), Lamb et al. (2019a), Piro et al. (2019), and Makhathini et al. (2020). Abbreviations: NIR, near-infrared; SED, spectral energy distribution.

these measurements rule out quasi-spherical outflows (see, e.g., Gill & Granot 2018, Granot et al. 2018a, Zrake et al. 2018 for simulations) and point to a compact radio source originating from a highly anisotropic outflow with average $\Gamma \approx \beta_{app} \approx 4$ around the time of afterglow peak. In the limit of a relativistically moving point source these observations also provided an estimate of the geometry of the dominant source of emission $(\theta_{obs} - \theta_{jet}) \sim 1/\Gamma \approx 0.25$. Supporting this scenario is the sharp light-curve peak at $t_{peak} \sim 160$ days followed by a steep achromatic $F_\nu \propto t^{-2.2}$ afterglow decay, which is naturally explained as the signature of the core of a narrow relativistic jet entering our line of sight and dominating the detected emission at $t \gtrsim t_{peak}$ (**Figure 7**). Radio observation at 244 days also indicate a degree of linear polarization $\Pi < 12\%$ (99% c.l., frequency of 2.8 GHz), which suggests that the postshock magnetic field cannot be fully contained within the shock plane (Corsi et al. 2018, Gill & Granot 2020).

This steep postpeak decay is consistent with the universal post-jet-break expectation from relativistic jets, $F_\nu \propto t^{-p}$, and contains no information on the jet collimation (Lamb et al. 2018). However, the rapid transition from peak to the asymptotic power-law decay on timescale

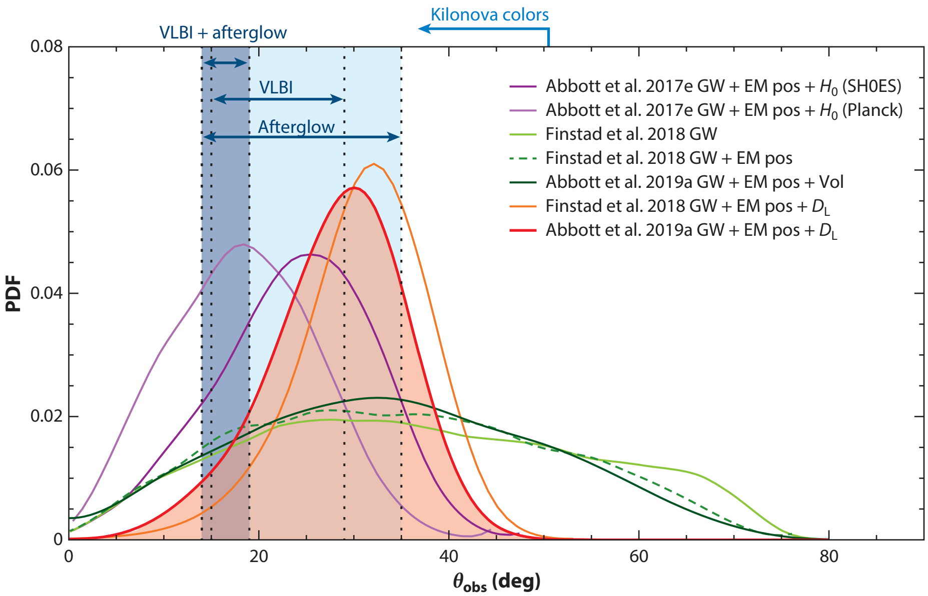

Figure 9

Constraints on θ_{obs} from GWs (*light green curve*) combined with different priors. The following are indicated: EM pos, subarcsec sky localization from the EM counterpart; D_L, Gaussian prior on the luminosity distance inferred by Cantiello et al. (2018); Planck or SH0ES H_0 values assumed from Planck Collab. et al. (2016) or Riess et al. (2016), respectively; and Vol, flat prior in volume (Abbott et al. 2017e, Finstad et al. 2018, Abbott et al. 2019a). Knowledge of the precise sky location has limited effect, whereas a prior on D_L (or H_0) strongly influences the inference on θ_{obs} (see also Mandel 2018, Chen et al. 2019). The difference between the Abbott et al. (2019a) and the Finstad et al. (2018) GW+EM pos+D_L posterior is related to slightly different choices of priors and frequency of the signal. Shaded blue areas show best-fitting ranges for θ_{obs} from the VLBI and afterglow modeling (Ghirlanda et al. 2019, Hotokezaka et al. 2019), from the VLBI-driven inferences of Mooley et al. (2018a), and for a variety of afterglow models that reproduce observations extending to $\delta t > 1$ year (Section 5). Abbreviation: EM, electromagnetic; GW, gravitational wave; PDF, probability density function; VLBI, very long baseline interferometry.

$\Delta t/t_{peak} \approx 1$–2 implies $\theta_{obs}/\theta_{jet} \approx 5$–6 (e.g., Nakar & Piran 2021, Ryan et al. 2020). When combined with the VLBI constraints, Mooley et al. (2018a), Ghirlanda et al. (2019), and Hotokezaka et al. (2019) find $\theta_{jet} \approx 2$–4 deg and $\theta_{obs} \approx 14$–19 deg (see also Gill & Granot 2018). The inferred θ_{obs} is consistent with inferences from the kilonova colors (Section 4) and GW modeling (Section 2; **Figure 9**). Similarly, being determined by the hydrodynamics of the deceleration of the jet core within the environment, $t_{peak} \propto (E_k/n)^{1/3}(\theta_{obs} - \theta_{jet})^{8/3}$ constrains the system parameters as $(E_k/n) \approx (1.5$–$1.9) \times 10^{53}$ erg cm^{-3} (Mooley et al. 2018a, Ghirlanda et al. 2019, Hotokezaka et al. 2019) when using the VLBI information (**Figure 10**). Importantly, the inferences so far do not depend on the poorly known shock microphysical parameters ϵ_e and ϵ_B.

Next, we consider the physical implications of the early afterglow evolution. The deep radio and X-ray nondetections at $\delta t \lesssim 2$ days (**Figures 7** and **11**) imply that the observer's line of sight is misaligned with respect to the jet core, i.e., $\theta_{obs} > \theta_{jet}$. However, the subsequent mild rise $F_\nu \propto t^{0.8}$ (**Figure 7**), which is significantly less steep than $F_\nu \propto t^3$, indicates that the observer was within the cone of emission of some outflow material with angular extent θ_w (Nakar & Piran 2018, Ryan et al. 2020) since the time of the first afterglow detection at ~9 days (Hallinan et al. 2017, Troja et al. 2017). Additionally, the rising afterglow emission before peak is sensitive to the ratio $\theta_{obs}/\theta_{jet}$

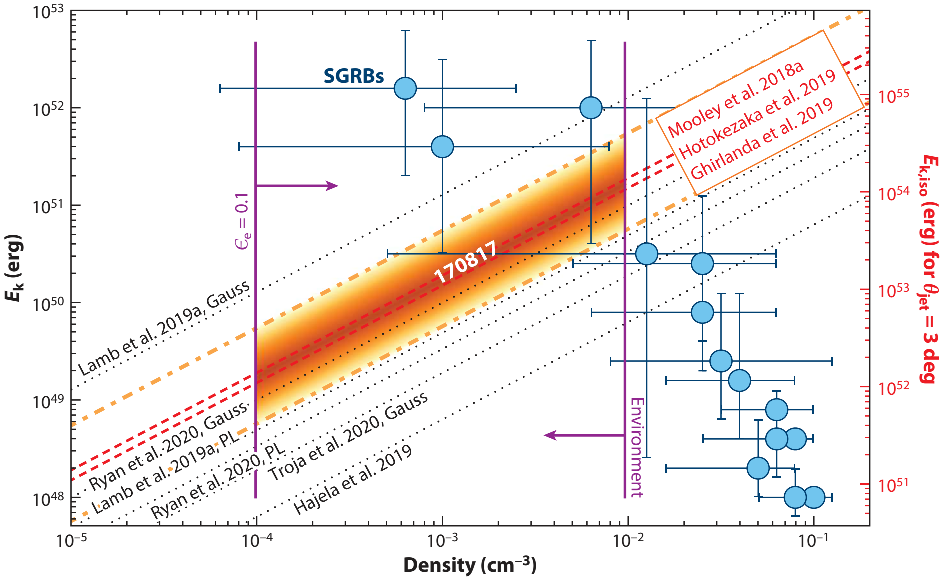

Figure 10

Constraints on the jet kinetic energy (beaming-corrected and isotropic equivalent) and environment density of GW170817 in the context of SGRBs. The red dashed lines and the orange dash-dotted lines mark the best-fitting values and their representative uncertainties from studies that self-consistently model the VLBI data and the afterglow data (Mooley et al. 2018a, Ghirlanda et al. 2019, Hotokezaka et al. 2019). Black dotted lines show best-fitting parameters from Hajela et al. (2019), Lamb et al. (2019a), Ryan et al. (2020), and Troja et al. (2020) (for power-law and Gaussian jets) that model the long-term evolution of the GW170817 afterglow under different assumptions. Blue circles show SGRBs from the homogeneous multiwavelength afterglow modeling by Wu & MacFadyen (2019), where no assumption is made on ϵ_e or ϵ_B. Colored area shows the likely $E_k - n$ range for GW170817 based on additional constraints from host-galaxy observations (Section 7) and theoretical expectations from the physics of particle acceleration in relativistic shocks (Section 5.1). Abbreviations: PL, power law; SGRB, short γ-ray burst; VLBI, very long baseline interferometry.

(Granot et al. 2018b, Nakar & Piran 2021, Ryan et al. 2020) and requires an increase of observed energy per unit time $E_{obs} \propto t^{1.3}$ (Nakar & Piran 2018, Pooley et al. 2018), which can be either the result of true energy injection into the shock [e.g., due to the deceleration of a radially stratified isotropic fireball with $\Gamma(r)$] or due to increasing energy per unit time that intercepts the observer's line of sight [i.e., apparent energy injection due to the progressive decrease of relativistic beaming of an anisotropic outflow with $\Gamma(\theta)$ and $E(\theta)$].

The combined evidence from the steep postpeak decay and VLBI observations rules out quasi-spherical radially stratified fireballs and points to an outflow with some angular structure, i.e., a structured jet. However, due to a massive degeneracy among $E(\theta)$, θ_{obs}, and $\Gamma(\theta, t)$, the prepeak afterglow light curve does not provide a unique $E(\theta)$ solution, in spite of being a direct manifestation of structure in the outflow (Ryan et al. 2020, Nakar & Piran 2021). For Gaussian jets with $E(\theta) \propto e^{-(\theta/\theta_{jet})^2}$ the observed rise implies $\theta_{obs}/\theta_{jet} \sim 5$–6, which is consistent with the findings above (Ryan et al. 2020). As a result, a variety of jet angular structures can adequately fit the afterglow data (**Figure 7**). These models are tuned to reproduce the afterglow data and are not necessarily sensitive to the tail of wider-angle mildly relativistic material that produced GRB 170817A (Section 3; Lamb & Kobayashi 2018, Ioka & Nakamura 2019).

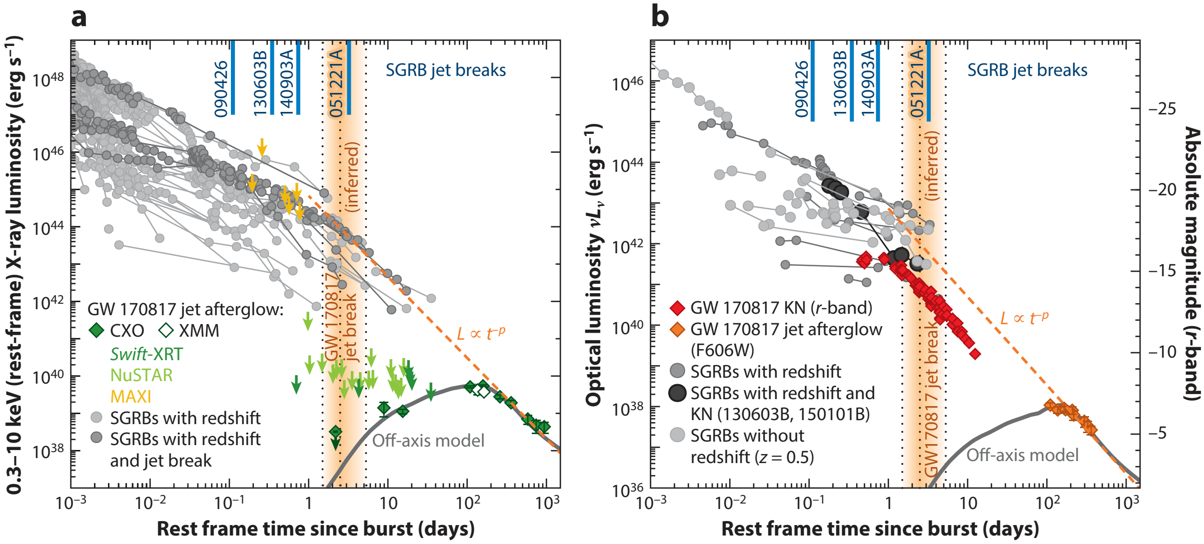

Figure 11

(*a*) X-ray and (*b*) optical GW170817 jet afterglow in the context of SGRB afterglows. Known SGRB jet-break times are indicated in blue, whereas the orange-shaded area marks the range of inferred jet-break times if GW170817 had been observed on axis. Interestingly, the back extrapolation of the postpeak, post-jet-break $L \propto t^{-p}$ evolution of GW170817 (*dashed orange line*) intercepts the luminosity of SGRB afterglows around the time of the inferred jet break, indicating that similar jet and environment properties are shared by GW170817 and SGRBs. The optical panel shows that the kilanova of GW170817 (*red diamonds*) typically would be outshined by the optical afterglow of an on-axis jet. The early *Swift*-XRT and NuSTAR limits acquired at $t < 2$ days with $L_x < 10^{40}$ erg s^{-1} clearly set GW170817 apart from cosmological SGRB afterglows. References: SGRBs: Burrows et al. (2006), Grupe et al. (2006), Evans et al. (2009), Fong et al. (2014, 2015, 2017), Troja et al. (2016, 2018b); GW170817: Evans et al. (2017), Sugita et al. (2018) and references of **Figure 7**. Abbreviations: CXO, *Chandra X-ray Observatory*; KN, kilonova; MAXI, Monitor of All-sky X-ray Image; NuSTAR, *Nuclear Spectroscopic Telescope*; SGRB, short γ-ray burst; VLBI, very long baseline interferometry; XMM, *X-ray Multi-Mirror Mission-Newton*; XRT, X-ray Telescope.

We conclude with a critical assessment of the insight offered by the afterglow data (Gill et al. 2019a, Beniamini et al. 2020b, Ryan et al. 2020, Nakar & Piran 2021). Detailed observations of the nonthermal emission in GW170817 provide uncontroversial evidence for the presence of an energetic, highly collimated relativistic jet with angular structure directed away from our line of sight and provide measurements of $\theta_{\rm obs}$, $\theta_{\rm jet}$, and p. Yet, these data leave the specific angular structure of the outflow at $\theta > \theta_{\rm obs}$ largely unconstrained. In particular, the angular extent of the jet wings, θ_w, is unknown. Additionally, even after a jet structure is assumed, the afterglow data effectively provide fewer constraints than the model parameters (i.e., the light curve, spectrum, and VLBI observations provide five constraints to the jet-core model versus at least seven model parameters: n, $E_{\rm k}$, $\theta_{\rm jet}$, $\theta_{\rm obs}$, ϵ_e, $\epsilon_{\rm B}$, p), which partially stems from the fact that the synchrotron spectral breaks ($\nu_{\rm sa}$, $\nu_{\rm m}$, $\nu_{\rm c}$) of the jet afterglow of GW 170817 fell outside the observed spectral window (e.g., Granot et al. 2018b, Gill et al. 2019a). A notable consequence is that though the ratio $E_{\rm k}/n$ is well constrained, as it effectively controls the outflow dynamics, the two parameters are not individually as well constrained by the jet afterglow modeling alone. Adding the independent inference on the environment density, $n < 0.01$ cm^{-3} (Section 7.1), leads to $E_{\rm k} < 10^{51}$ erg, which is independent from the shock microphysical parameter values. ϵ_e and $\epsilon_{\rm B}$ are loosely constrained by the requirement $\nu_{\rm c}(t_{\rm peak}) > \nu_{\rm X}$, which leads to $n \lesssim 2 \times 10^{-6} \epsilon_{\rm B}^{-1}$ cm^{-3} and by the observed flux at peak $F_{\nu,\,\rm peak}(\nu)$, which links n, $\epsilon_{\rm B}$, and ϵ_e. Taking $n \sim 10^{-3}$ cm^{-3} as a fiducial density value in early-type galaxies, the relations above suggest small $\epsilon_{\rm B} < 10^{-3}$. Specifically, for $\epsilon_e = 0.1$ (a robust prediction from simulations of particle acceleration by relativistic shocks; e.g., Sironi et al. 2013), $n \gtrsim 10^{-4}$ cm^{-3} and $\epsilon_B \lesssim 4 \times 10^{-4}$ (**Figure 10**).

Additionally, because the transition from the coasting phase to the deceleration phase of the jet core was not observed, the initial jet-core Lorentz factor Γ_0 after breakout is fundamentally unconstrained (from VLBI observations, $\Gamma_0 > 4$). A further constraint on the system will be provided by the transition to the nonrelativistic (NR) regime (Section 5.4) that leads to an achromatic flattening of the afterglow light curve as the outflow enters the Sedov phase and becomes spherical, and the emission from the counter-jet enters our line of sight. However, other components of emission might outshine the jet afterglow by this time (Section 8.1).

5.2. A Physically Motivated Structured-Jet Model

Structured relativistic outflows are a natural outcome of BNS mergers (Section 1.4), and the outflow's structure (radial and/or angular) and collimation can be imparted by the jet acceleration process [e.g., Kathirgamaraju et al. (2019b) in the context of MHD-driven jets] or by the hydrodynamical interaction of the jet with the merger's debris cloud consisting of winds and dynamical ejecta (see references in Section 1.4; Kasliwal et al. 2017b; Lazzati et al. 2017b, 2018; Murguia-Berthier et al. 2017b; Duffell et al. 2018; Gottlieb et al. 2018b, 2021; Nakar et al. 2018; Xie et al. 2018; Lazzati & Perna 2019) or both (Bromberg et al. 2018). The presence of heavy dynamical ejecta along the rotation axis, and the subsequent jet interaction, might have played a primary role in the jet collimation process in GW170817, which has been a long-standing theoretical problem in BNS mergers (Nagakura et al. 2014, Duffell et al. 2015). In this context, other key parameters determining the angular structure of the outflow and how the energy is partitioned within the outflow are the delay (if any) between the BNS merger and jet launching, as well as the time the engine remains active after jet breakout (e.g., Murguia-Berthier et al. 2017b, 2021; Geng et al. 2019; Lazzati & Perna 2019; Beniamini et al. 2020a). The structure of the fastest outflows from BNS mergers thus encodes information about the NS equation of state (EoS), the nature of the remnant (if launch of a jet requires the collapse to form a BH), and the jet launching mechanism.

Recent simulations of BNS mergers listed above have shown that the process involving a light jet trying to pierce through the dense merger ejecta leads to two potential outcomes: The jet is stalled within the ejecta and no collimated ultrarelativistic outflow survives or, alternatively, more energetic jets or jets that encounter less mass enveloping the polar regions can survive the interaction and break through the merger ejecta, launching powerful jets in the circum-merger environment. For both successful and failed jets, the propagation of the jet within the merger ejecta creates a mildly relativistic ($\Gamma < 10$) wide-angle cocoon with energy E_c proportional to the time spent by the jet within the ejecta (e.g., Ramirez-Ruiz et al. 2002). The jet energy E_k is proportional to the time the engine remains active after the jet breaks out from the merger ejecta. In the case of failed jets, the resulting outflow consists of a pure cocoon (i.e., a wide angle, $\theta \gtrsim 30$ deg, mildly relativistic outflow). In the case of successful jets, the resulting outflow consists of a jet+cocoon system, with a narrow ($\theta_{jet} \sim$ a few degrees) highly relativistic core surrounded by a sheath of mildly relativistic material at $\theta > \theta_{jet}$. Because the quenching (or survival) of the jet is not theoretically guaranteed, both options are equally viable until observational evidence contradicts the expectations from either class of models.

The afterglow observations of GW170817 (Section 5.1) establish that some BNS mergers are able to launch relativistic jets that survive the interaction with the merger debris cloud (ejecta and winds) while also powering wide-angle outflows with energy E_c comparable with the jet energy E_k. Although different jet structures can adequately explain the afterglow data (**Figure 7**), the jet+cocoon system, with a built-in mechanism for dissipation of energy into γ-rays, also self-consistently accounts for GRB 170817A (Section 3), and thus constitutes a natural physical model for GW170187. Conversely, the observed nonthermal afterglow of GW170817 is not consistent with quasi-spherical models including magnetar-like giant flares (Salafia et al. 2018), the interaction of the fast tail of the dynamical ejecta with the environment (Hotokezaka et al. 2018), and pure cocoon systems (i.e., a failed-jet scenario) that were viable options until the emission from the jet core entered our line of sight at ∼160 days (e.g., Kasliwal et al. 2017b, Mooley et al. 2018a, Nakar & Piran 2018, Nakar et al. 2018).

5.3. Connection to Short Gamma-Ray Burst Afterglows

Observations of SGRB afterglows in the past decade provide a remarkable basis for comparison with GW170817, which represents the first bona fide detection of a broadband afterglow from an off-axis ultrarelativistic jet launched by a BNS merger. SGRBs harbor relativistic jets with similar energy ($E_k \approx 10^{48}$–10^{52} erg) viewed on axis (with the likely exception of SGRB 150101B; Troja et al. 2018b) and propagating into similarly low-density environments ($n \approx 10^{-4}$–10^{-1} cm^{-3}; Berger 2014, Fong et al. 2015, Wu & MacFadyen 2019).

Following Fong et al. (2019), we first proceed with a simple, yet model-agnostic, exercise. We place the afterglow of GW170817 in the luminosity phase space of SGRBs in **Figure 11**. A few considerations follow. (*a*) With detections extending to 940 days since merger, the proximity of GW170817 is allowing us to explore a phase of the afterglow evolution that we have never sampled before. (*b*) Optical kilonovae are typically outshined by on-axis optical afterglows. (*c*) The overlap between AT 2017gfo and the faintest optical afterglows allows for the possibility that some SGRBs are viewed slightly off axis (Fong et al. 2019), similar to SGRB 150101B (Burns et al. 2018, Troja et al. 2018b). (*d*) Although we know the radio evolution of GW170817 in striking detail, we only have sparse radio light curves of 9 SGRBs after ∼15 years of investigations (Fong et al. 2020). Common to all the spectral wavelengths is the faintness of the off-axis afterglows relative to the sensitivity of current instrumentation: The GW170817 afterglow at peak would only be detectable to within $\lesssim$160 Mpc by the most sensitive X-ray and radio observatories (e.g., Gottlieb et al. 2019).

Second, we extrapolate back in time the postpeak afterglow evolution $F_\nu \propto t^{-2.2}$, which is entirely dominated by the jet-core component (Section 5.1). This behavior is consistent with the $F_\nu \propto t^{-p}$ expectation from the post-jet-break dynamics of a jet with sideways expansion, which predicts universal afterglow light curves that depend on the true jet energy (rather than on its isotropic equivalent value) and carries no dependency on the system geometry (i.e., $\theta_{\rm jet}$ and $\theta_{\rm obs}$; e.g., Granot et al. 2018b). **Figure 11** shows that the extrapolation of the postpeak evolution of the jet afterglow of GW170817 does intersect with the SGRB afterglow population at their expected and/or measured jet-break times. This is consistent with the notion that GW170817 and cosmological SGRBs share similar combinations of true jet-core energetics, circumburst density, and shock microphysics. Variations of these extrinsic and intrinsic properties contribute to the diversity of SGRB afterglows post jet-break, whereas viewing angle effects are primarily responsible for the observed differences in the early-time broadband temporal evolution of SGRBs and the afterglow of GW170817.

This comparison suggests that jets that successfully pierce through the merger debris might have similar ultrarelativistic core energetics (see Salafia et al. 2019 and Wu & MacFadyen 2019 for a detailed calculation of the on-axis afterglow). However, no conclusion can be drawn regarding the universality of the angular structure of the outflow, because in SGRBs the emission from the jet core likely dominates at all times (with no detectable contribution from the wings). The universality of the jet structure is an important open question that directly connects the merger conditions and outcome (i.e., if and when a jet is launched, what the amount and distribution of ejecta and wind material along the jet path will be; Section 5.2), which depend on the NS EoS, and the accretion physics, which sets the accretion-to-jet energy conversion efficiency, and hence the jet energy reservoir (e.g., Salafia & Giacomazzo 2020).

Finally, we consider the jet collimation of GW170817 compared with that of SGRBs and the fraction of successful jets in BNS mergers. SGRB jet opening angles measured from afterglow jet-breaks are in the range of $\theta_{\rm jet}^{\rm SGRB} \sim 3$–8 deg (Fong et al. 2015, Lamb et al. 2019b, Troja et al. 2019a). The $\theta_{\rm jet}^{\rm SGRB}$ measurements are biased against less collimated jets that would break at later times and fainter fluxes not covered by observations. A few SGRBs have jet-break times lower limits indicative of wider jets with $\theta_{\rm jet}^{\rm SGRB} \gtrsim 13$–25 deg (e.g., SGRBs 050709, 050724A, and 120804A). In any case, with $\theta_{\rm jet} \approx 2$–4 deg, GW170817 lies in the highly collimated end of the SGRB jet-angle distribution. These properties, together with current GW constraints on BNS mergers, indicate that >10% of BNS mergers launch collimated jets that successfully pierce through the merger debris cloud (Ghirlanda et al. 2019), with this fraction potentially extending to ≈100% (**Figure 3**; see also Beniamini et al. 2019). However, the combination of the high level of collimation and intrinsic or apparent faintness of the wide-angle and off-axis γ-ray emission, respectively, and sensitivity of the current instrumentation implies that only 1–10% of GW-discovered BNS mergers will have a detected γ-ray counterpart (Beniamini et al. 2019).

Tidal deformability parameters (Λ): $\Lambda \equiv \frac{2}{3} k_2 \left(\frac{c^2}{G} \frac{R}{m}\right)^5$, where k_2 is the dimensionless $\ell = 2$ Love number and R and m are the NS radius and mass

5.4. Other Potential Sources of Nonthermal Emission at t < 1,000 Days

Radiation from a long-lived central engine such as an accreting BH or a millisecond magnetar has been invoked in SGRBs to power their extended emission (e.g., Metzger et al. 2008), X-ray flares (Margutti et al. 2011), and X-ray light-curve plateaus, as well as the late-time excess of X-rays of SGRB 130603B (Fong et al. 2014, Kisaka et al. 2016). The X-ray optical depth through the merger ejecta of density $\rho_{\rm ej}$, mass $M_{\rm ej}$, and radius $R_{\rm ej} \sim v_{\rm ej} t$ is $\tau_{\rm X} \simeq \rho_{\rm ej} R_{\rm ej} \kappa_{\rm X} \approx 2 \times 10^4 (\kappa_{\rm X}/1{,}000\,{\rm cm^2\,g^{-1}})(M_{\rm ej}/10^{-2}\,{\rm M_\odot})(v_{\rm ej}/0.2\,{\rm c})^{-2}(t/1\,{\rm day})^{-2}$, where $\kappa_{\rm X} \sim 1{,}000\,{\rm cm^2\,g^{-1}}$ is the bound-free opacity of neutral or singly ionized heavy r-process nuclei at ∼1–10 keV (e.g., Metzger 2019). For centrally produced X-rays to be able to leak out, either $\tau_{\rm X} < 1$ or the ejecta material needs to be fully ionized, which requires $L_x \sim 10^{43}$–$10^{44}\,{\rm erg\,s^{-1}}$ (e.g., Metzger & Piro 2014). Because neither of these conditions is met by GW170817 at $t < 150$ days (e.g., Pooley et al. 2018), it is unlikely that radiation from the merger remnant dominates the X-ray energy release at those early epochs. The remarkably constant ratio of the X-ray to radio luminosity of GW170817 from 9 days to ∼750 days since merger (**Figure 8**) and the lack of statistically significant X-ray variability (Hajela et al. 2019) independently argue against a magnetar and/or BH origin of the detected X-rays at all times. Searches for short-term X-ray flux variability in future BNS mergers have the potential to uncover sudden reactivations of the central engine (Piro et al. 2019).

6. MULTIMESSENGER GRAVITATIONAL WAVE + ELECTROMAGNETIC INFERENCES

6.1. Deformability, Ejection of Matter, and the Nature of the Colliding Stars

The tidal deformability parameters Λ_1 and Λ_2 of the two compact objects describe the amount of deformation of matter. The tidal field of the binary companion induces a mass-quadrupole moment in an NS with observable effects in the GW emission that become more prominent as the orbital separation approaches the NS radius R.

The dimensionless Λ parameters are proportional to the induced quadrupole moment and quantify the strength of these effects. Because Λ directly depends on the mass and radius of an NS, a measurement of Λ directly probes and constrains the EoS of nuclear matter, as well as the intrinsic nature of the merging compact objects, as $\Lambda = 0$ for a BH. Inferences on the deformability of matter can be derived from both GWs and EM emission. We first review the constraints on Λ_1 and Λ_2 placed by GW measurements alone, and then discuss the additional inferences enabled by the detection of EM radiation from this system.

Mass-weighted deformability parameter ($\tilde{\Lambda}$): $\tilde{\Lambda} \equiv \frac{16}{13}\frac{(m_1+12m_2)m_1^4\Lambda_1}{(m_1+m_2)^5} + \frac{16}{13}\frac{(m_1+12m_2)m_2^4\Lambda_2}{(m_1+nm_2)^5}$; leading tidal contribution to the GW phase evolution defined such that $\tilde{\Lambda} = \Lambda_1 = \Lambda_2$ for $m_1 = m_2$

Assuming no correlation between Λ_1 and Λ_2 and allowing the two parameters to vary independently, Abbott et al. (2019a) derive a system mass-weighted deformability parameter of $\tilde{\Lambda} \in (0, 630)$ (90% lower and upper limit range) for the high-spin prior ($\chi \leq 0.89$) and $\tilde{\Lambda} = 300^{+420}_{-230}$ (90% highest posterior density interval) for the low-spin prior ($\chi \leq 0.05$) that is consistent with known Galactic NSs that would merge within a Hubble time. This result rules out at the 90% c.l. several EoS models (Abbott et al. 2019a, their figure 10). The $\tilde{\Lambda}$ posterior has some support at $\tilde{\Lambda} = 0$ primarily associated with binaries with low-mass ratio $q = m_2/m_1 \lesssim 0.5$. Interestingly, for $q \approx 1$, which is typical of the known population of Galactic BNSs, $\tilde{\Lambda} = 0$ lies outside the 90% c.l. region of the low-spin and high-spin $\tilde{\Lambda}$ posteriors, and the two posteriors are very similar. Only for the low-spin prior the posterior of $\tilde{\Lambda} = 0$ has no support within the 90% c.l. for any q value. The individual posteriors of Λ_1 and Λ_2 have support at $\Lambda_1 = \Lambda_2 = 0$ at 90% c.l. for both the high-spin and low-spin priors. The conclusion is that with minimal assumptions on the intrinsic nature of the merging objects built into the priors, and based on GWs alone, it is not possible to definitely assert that both colliding objects are NSs (Abbott et al. 2019a, 2020b): A BNS merger is the most likely scenario for GW170817, but BH–BH and NS–BH systems are statistically allowed.

A reasonable assumption is that both objects obey the same (unknown) EoS, which is equivalent to assuming that Λ_1 and Λ_2 are in fact correlated and have similar values for similar NS masses. Working under this hypothesis and further assuming that the two NSs have spins in the range of those of Galactic BNSs lead to a substantial improvement on the $\Lambda_1 - \Lambda_2$ credibility region (Abbott et al. 2018, their figure 1). For an NS with mass of $1.4\,M_\odot$, $\Lambda_{1.4} = 190^{+390}_{-120}$ at the 90% c.l., favoring soft rather than stiff EoSs. With the addition of EoS-insensitive relations among macroscopic properties of NSs that allow mapping of tidal deformabilities into NS radii, Abbott et al. (2018) derive primary (heavier) NS areal radii of $R_1 = 10.8^{+2.0}_{-1.7}$ km and $R_2 = 10.7^{+2.1}_{-1.5}$ km for the lighter NS. Further enforcing the EoS to support a maximum NS mass $\geq 1.97\,M_\odot$ to match the mass of the heaviest NS known ($M = 2.01 \pm 0.04\,M_\odot$; Antoniadis et al. 2013), the radii constraints improve to $R = 11.9^{+1.4}_{-1.4}$ km for both components, which is consistent with the results by De et al. (2018a,b) and Most et al. (2018).

The multiple EM counterparts of GW170817 and their associated outflows (jet, kilonova; Sections 4 and 5) are a direct manifestation of the presence and ejection of matter, which ultimately implies that at least one compact object is an NS. Several approaches have been used in the literature to combine the evidence from GWs and EM radiation into inferences on $\tilde{\Lambda}$, the NS EoS, NS radii, and the maximum mass of a cold spherical nonrotating NS ($M_{\rm TOV}$, i.e., the TOV or Tolman–Oppenheimer–Volkoff limit). Considerations on the total energetics of the EM outflows (kilonova+jet) on the order of $\approx 10^{51}$ erg (Sections 4 and 5), which place a direct constraint on the budget of extractable energy from the rapidly rotating merger remnant, together with the constraints on the kilonova ejecta masses, the presence of the blue kilonova component, and the system total mass derived from GWs have been employed by Margalit & Metzger (2017), Shibata et al. (2017), Rezzolla et al. (2018), and Ruiz et al. (2018) to derive credibility intervals of $M_{\rm TOV}$, found to be in the range of 2.01–2.33 $M_\odot$. Relaxing the assumption of an initially rapidly rotating remnant leads to $M_{\rm TOV} \lesssim 2.3\,M_\odot$ (Shibata et al. 2019, Rezzolla et al. 2018).

EM observations of the kilonova can also be used to inform our inferences on $\tilde{\Lambda}$ values derived from GW data. Expanding on work by Radice et al. (2018c), Radice & Dai (2019) infer $\tilde{\Lambda} \gtrsim 300$ based on a lower limit of $0.04\,M_\odot$ on the merger remnant disk mass that is necessary to support accretion disk winds powerful enough to deposit the observed kilonova ejecta mass.

Similarly, Coughlin et al. (2018, 2019) derive $\tilde{\Lambda} > 300$ and $m_1/m_2 \in (1,1.27)$ at 90% c.l. The inclusion of EM inference in the analysis of GW170817 thus lowers the support around the BH–BH region of the parameter space ($\tilde{\Lambda} = 0$). (Astrophysical support for BH–BH systems with the very small masses inferred for GW170817 is scarce based on our current understanding of stellar evolution.) However, though a BNS merger is favored, a joint EM+GW analysis leaves open the possibility of an NS–BH system (e.g., Coughlin & Dietrich 2019, Hinderer et al. 2019) unless at least some of the blue kilonova material originated from shock-heated ejecta at the interface of the two colliding NSs or a neutrino-driven wind from a remnant HMNS. Finally, these hybrid EM+GW approaches also enable estimates of NS radii that are more precise than those based on pure GW analyses (e.g., Bauswein et al. 2017). For example, Radice & Dai (2019) derive $R(1.4\,M_\odot) = 12.2^{+1.0}_{-0.8} \pm 0.2$ km (90% c.l., statistical and systematic uncertainties). The addition of nuclear physics constraints allowed Capano et al. (2020) to obtain $R(1.4\,M_\odot) = 11.0^{+0.9}_{-0.6}$ km (90% c.l.).

In summary, these multimessenger endeavors are ultimately enabled by the fact that, physically, the merger process, the postmerger remnant evolution, the mass-ejection process, and the ejecta mass properties (as well as the properties of the emerging ultrarelativistic jet) fundamentally depend on the NS EoS. At the time of writing, their major limitation is related to the level of advancement of current models of the EM signal, which in most cases rely on a set of numerical relativity simulations that do not cover the entire parameter space (e.g., Kiuchi et al. 2019). A larger sample of BNS mergers with EM+GW detections and an improved quantitative understanding of the EM emission are necessary to realize the full scientific potential of multimessenger parameter estimation in future work. This is the current leitmotif of joint EM+GW studies of compact-object mergers.

6.2. Precision Cosmology with Gravitational Waves and Their Electromagnetic Counterparts

GW sources offer a standard siren measurement of H_0 (Schutz 1986) that is independent of a cosmic distance ladder, does not assume a cosmological model as a prior, and is thus well positioned to resolve the current tension between the *Planck Surveyor Satellite* and the Cepheid-SN measurements of H_0 (Planck Collab. et al. 2016, Riess et al. 2019). The additional constraints provided by the redshift of the galaxy hosting the GW event have been explored and quantified by Holz & Hughes (2005) and Nissanke et al. (2010, 2013) in the context of H_0.

Using the sky position of AT 2017gfo and combining the recession velocity derived from the redshift (and peculiar velocity) of the host galaxy NGC 4993 with the distance to the source derived from GW data, Abbott et al. (2017e) infer $H_0 = 70.0^{+12.0}_{-8.0}$ km s^{-1}Mpc^{-1} (1σ). A reanalysis of the GW data led Abbott et al. (2019a) to slightly revised values, which are listed in **Table 1**. It is estimated that ~60–200 GW-detected BNS mergers with identified host galaxies will lead to a precision measurement of H_0 at the level of 2–1% (Chen et al. 2018; see also Feeney et al. 2019). At the time of writing, this is one of the most promising venues that might clarify the discrepancy between existing local (i.e., Type Ia SNe) and high-z (CMB) H_0 measurements.

For these multimessenger measurements of H_0 the major source of uncertainty is the degeneracy between the luminosity distance and the inclination angle of the binary, which is intrinsic to GW data of BNS mergers (Abbott et al. 2017e, Chen et al. 2019). The jet afterglow provides an independent measure of the observing angle (Section 5). Assuming that the jet is aligned with the binary rotation axis, this information can be used to solve the GW parameter degeneracy (Guidorzi et al. 2017). Using this additional constraint on θ_{obs}, the precision of the H_0 multimessenger measurement improves by a factor of about two (Hotokezaka et al. 2019, Wang

Table 1 H_0 values derived from multimessenger analysis of GW170817[a]

Method	H_0 ($\mathrm{km\,s^{-1}\,Mpc^{-1}}$)[b]	Model	Reference
GW+EM position+HG[c]	70^{+13}_{-7}	High-spin case	Abbott et al. 2019a
GW+EM position+ HG	70^{+19}_{-8}	Low-spin case	Abbott et al. 2019a
GW+EM position+ HG + θ_{obs}	$70.3^{+5.3}_{-5.0}$	Hydrodynamical jet	Hotokezaka et al. 2019[d]
GW+EM position+ HG + θ_{obs}	$68.1^{+4.5}_{-4.3}$	Power-law jet	Hotokezaka et al. 2019
GW+EM position+ HG + θ_{obs}	$68.3^{+4.4}_{-4.3}$	Gaussian jet	Hotokezaka et al. 2019
GW+EM position+ HG + θ_{obs}	$69.5^{+4.0}_{-4.0}$	MHD jet	Wang & Giannios 2021
Planck (CMB)	67.74 ± 0.46[e]	TT, TE, EE + lowP + lensing + ext[f]	Planck Collab. et al. 2016
SH0ES (Ia SNe)	73.24 ± 1.74	NA	Riess et al. 2016
SH0ES+LMC Cepheids	74.03 ± 1.42	NA	Riess et al. 2019

[a]The first two rows list H_0 estimates based on GW data, the sky position of the EM counterpart, and the HG redshift. The following four rows combine the inferences on the observing angle derived from the afterglow (Section 5). The CMB and local-distance ladder estimates of H_0 are also listed for ease of comparison.

[b]1σ credible intervals listed.

[c]All the methods listed here assume a peculiar velocity $v_{\mathrm{p}} = 310 \pm 170\ \mathrm{km\,s^{-1}}$ for NGC 4993. Note, however, that Hjorth et al. (2017) and Guidorzi et al. (2017) independently estimate a larger uncertainty $\sigma_{v_{\mathrm{p}}} \sim 230$–$260\ \mathrm{km\,s^{-1}}$ that would contribute additional uncertainty to H_0 (Abbott et al. 2017e, their extended data figure 2).

[d]Favored model.

[e]Planck base ΛCDM value.

[f]TT, EE, TE, etc., are the names of the models taken from the reference. TT, TE, EE: Planck CMB power spectra; here TT represents temperature power spectrum, TE is temperature-polarization cross spectrum, and EE is polarization power spectrum. lowP, Planck polarization data in the low-ℓ likelihood; lensing, CMB lensing reconstruction; ext, external data (BAO+JLA+H0).

Abbreviations: BAO, baryon acoustic oscillations; CMB, cosmic microwave background; EM, electromagnetic; GW, gravitational wave; HG, host galaxy; JLA, joint light-curve analysis (of supernovae); H_0, Hubble constant; MHD, magnetohydrodynamic; NA, not applicable.

& Giannios 2021). The accuracy of the method relies on the modeling of the EM afterglow data and on specific assumptions to interpret the data (e.g., the assumed jet structure, modeling of the hydrodynamical jet spreading, etc.). These EM systematics currently constitute the major limitation of this method and dominate over the GW systematics, which are primarily related to the instrumental calibration error in the amplitude of the signal (e.g., Chen et al. 2019). Although adding a new source of systematics and being limited to bright afterglows in the nearby Universe ($d \lesssim 100$ Mpc) where the afterglow can be imaged, detected, and well sampled, this method brings the benefit of significantly reducing the number of BNS mergers necessary for 1%-precision measurements of H_0 to $\mathcal{O}(10)$ (Chen et al. 2019, Hotokezaka et al. 2019).

6.3. Tests of General Relativity and Fundamental Physics

The joint detection of gravitational and electromagnetic waves from the same celestial body enables powerful new ways to test GR and fundamental physics. The measured delay between GWs and γ-rays of $\Delta t_{\mathrm{GW}-\gamma} = 1.74 \pm 0.05$ s (Section 3.2) constrains the difference between the speed of gravity c_{g} and the speed of light c as $-3 \times 10^{-15} \leq (c_{\mathrm{g}}/c - 1) \leq 7 \times 10^{-16}$ (Abbott et al. 2017b, Shoemaker & Murase 2018). This multimessenger measurement places new bounds on the violation of Lorentz invariance and offers a new test of the equivalence principle by probing whether EM and gravitational radiation are equally affected by the background gravitational potential, which can be quantified with an estimate of the Shapiro delay (Abbott et al. 2017b, Wei et al. 2017, Boran et al. 2018). The tight $|c_{\mathrm{g}}/c - 1|$ constraint severely limits the parameter space of modified theories of gravity that offer alternative gravity-based explanations to dark energy or are dark matter "emulators" (Baker et al. 2017, Creminelli & Vernizzi 2017, Ezquiaga & Zumalacárregui 2017, Sakstein & Jain 2017, Boran et al. 2018, de Rham & Melville 2018, Dima & Vernizzi 2018, Langlois et al. 2018). Additionally, the comparison between the EM and GW distance of GW170817 allows inferences to be drawn regarding the presence of additional large spacetime dimensions, which are found to be consistent with the GR prediction of $D = 4$ (Pardo et al. 2018, Abbott et al. 2019b). Finally, the NS coalescence GW signal enables tests on the deviation from the general-relativistic dynamics of the source and on the propagation and polarization of GWs (Abbott et al. 2019b). No significant deviation from GR expectations has been found.

7. ENVIRONMENT

7.1. Host-Galaxy Properties and Properties of the Local Environment

GW170817 was localized at a projected offset of 10.315 ± 0.007 arcsec (2.162 ± 0.001 kpc) from the center of the S0 galaxy NGC 4993 (**Figure 12**; e.g., Blanchard et al. 2017, Im et al. 2017, Kasliwal et al. 2017b, Levan et al. 2017, Palmese et al. 2017, Pan et al. 2017). NGC 4993 is well modeled by an $n \approx 4$ Sérsic profile and shows a strong bulge component as well as a complex morphology of dust lanes, concentric shells, and spiral features that indicate a relatively recent ($\lesssim$1 Gyr) galaxy merger. The global SED of NGC 4993 has been fitted with multiple methods, assumptions and data sets (e.g., Blanchard et al. 2017, Pan et al. 2017) leading to a concordant picture of a massive galaxy [stellar mass $\log(M_*/\mathrm{M}_\odot) = 10.65^{+0.03}_{-0.03}$] with an old stellar population (half-mass assembly time $\tau_{1/2} = 11.2^{+0.7}_{-1.4}$ Gyr) and limited ongoing star formation [$\log(\mathrm{SFR}/\mathrm{M}_\odot\,\mathrm{year}^{-1}) = -2.00^{+0.44}_{-0.66}$]. Due to higher SFR at early times, 90% of the total stellar mass was formed by $\sim 6.8^{+2.2}_{-0.8}$ Gyr ago. Additionally, the emission-line properties are consistent with the presence of a weak active galactic nucleus (AGN) revealed by nuclear X-ray and radio emission in significant excess of the inferred star formation [$L_X \approx (2\text{–}3) \times 10^{39}$ erg s^{-1} (0.5–8 keV), $L_{6\mathrm{GHz}} \approx 7 \times 10^{26}$ erg s^{-1} Hz^{-1}; Blanchard et al. 2017, Levan et al. 2017]. The early-type morphology of NGC 4993 is similar to ~1/3 of SGRB host galaxies and the presence of AGN activity is not unprecedented among SGRB host galaxies. NGC 4993 is superlative among SGRB host galaxies because of its very old stellar population age and exceedingly low SFR (Fong et al. 2017).

Next, we constrain the properties of the BNS merger's local environment with optical, radio, and X-ray observations of NCG 4993. GW170817 is located within the half-light radius of its host galaxy ($R \sim 0.6 r_\mathrm{e}$, where r_e is the Sérsic effective radius; Blanchard et al. 2017, Levan et al. 2017, Pan et al. 2017), at a relatively bright location and relatively close to the host-galaxy center. As a comparison, ≈75–80% of SGRBs are localized in fainter regions of their host galaxies and ≈25% of SGRBs are more proximal to their host centers (**Figure 12**; Fong et al. 2017). Constraints on the local environment density of GW170817 can be placed by radio observations that probe the H I surface density and by X-ray observations of bremsstrahlung emission from hot plasma in the host galaxy, which probe the presence of ionized H. Hallinan et al. (2017) infer a local number density of neutral H, $n_{\mathrm{H\,I}} < 0.04\,\mathrm{cm}^{-3}$, whereas Hajela et al. (2019) infer $n_{\mathrm{H}^+} < 0.01\,\mathrm{cm}^{-3}$ (3σ c.l.) from diffuse X-ray emission at the location of GW170817 (which is consistent with the less constraining limit on n_{H^+} reported by Makhathini et al. 2020). Deep HST observations acquired at $\delta t \approx 584$ days (after the afterglow had completely faded away) rule out preexisting emission from point sources with absolute $M_{\mathrm{F606W}} < -4.8$ mag at the transient location (Fong et al. 2019). These findings offer independent support for the low-density environment suggested by the afterglow studies (Section 5.1). The global properties of NGC 4993 and the properties of the transient location are thus consistent with those of the population of SGRBs, and in line with expectations for BNS mergers.

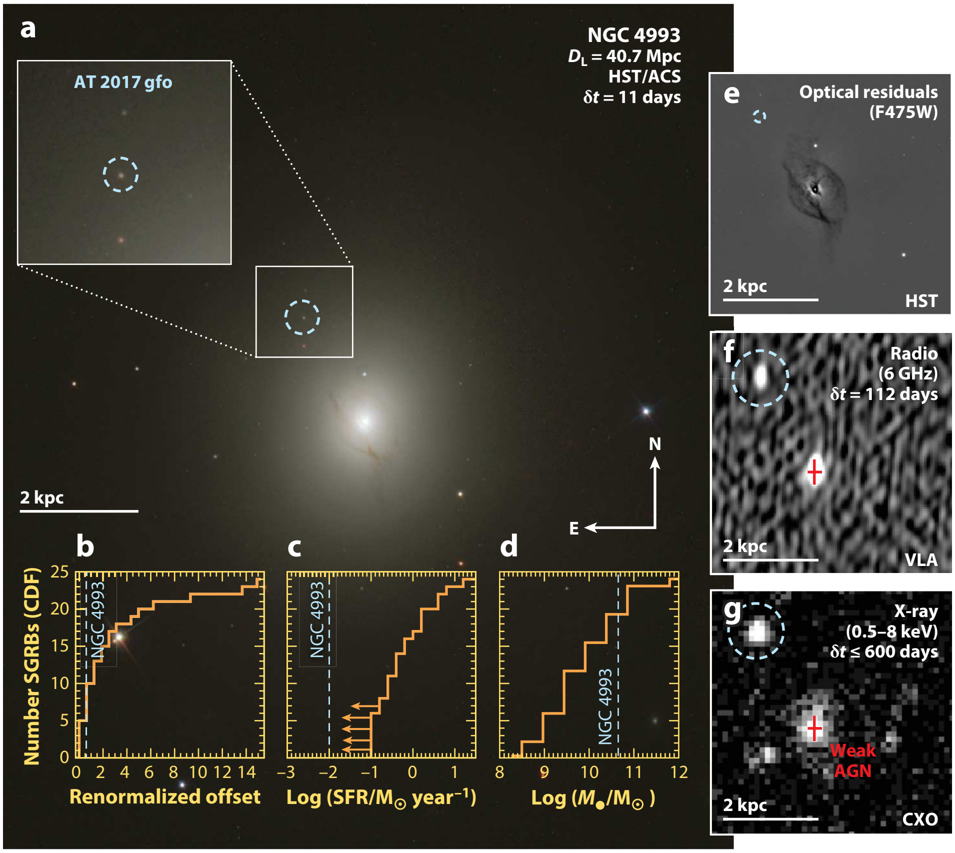

Figure 12

(*a*) Color image of NGC 4993 created from filtered HST/ACS images (F850LP, F625W, F475W) acquired at $\delta t \approx 11$ days by Blanchard et al. (2017). The location of the EM counterpart to GW170817 is identified by a dashed light-blue circle. Inferred properties of NGC 4993 (Section 7) compared with the (*b*) renormalized offset, (*c*) SFR, and (*d*) stellar mass distributions of host galaxies of SGRBs from Leibler & Berger (2010), Berger (2014), Fong et al. (2017) and Nugent et al. (2020). (*e*) Residual image in the HST ACS/F475W filter after the subtraction of a Sérsic brightness profile with $n \approx 4$ showing the presence of dust lanes around the host nucleus (from Blanchard et al. 2017). (*f*) Radio (VLA, 6 GHz) and (*g*) X-ray (CXO, 0.5–8 keV) images of the field acquired when the jet afterglow is clearly detectable. Radio and X-ray emission from a weak AGN is also present and marked with a red cross (observations published by Alexander et al. 2018, Margutti et al. 2018, Hajela et al. 2019). Abbreviations: ACS, Advanced Camera for Surveys; AGN, active galactic nucleus; CDF, *Chandra* Deep Field; CXO, *Chandra X-ray Observatory*; EM, electromagnetic; HST, *Hubble Space Telescope*; SFR, star-formation rate; VLA, Very Large Array.

7.2. Implications for the Progenitor Formation

We explore the inferences on the progenitor formation of GW170817 that can be drawn from the properties of its global and local environment (Section 7.1). The final BNS merger location depends on a combination of factors (e.g., Abbott et al. 2017c), including (*a*) the location of initial formation and the binary formation channel (e.g., dynamical versus binary stellar evolution); (*b*) initial binary properties, which determine the binary evolutionary path and the NS masses; (*c*) the systemic velocity of the binary after the second SN explosion, which imparts an SN kick to the newly formed NS and a mass-loss kick on the companion NS; and (*d*) host-galaxy gravitational potential where the binary moves.

There is no observational evidence that supports a dynamical formation scenario of the GW170817 progenitor in a globular cluster (GC: Blanchard et al. 2017, Levan et al. 2017, Pan et al. 2017, Lamb et al. 2019a). Deep HST observations obtained at $\delta t \approx 584$ days place a luminosity limit of $\lesssim 6.7 \times 10^3\ L_\odot$ ($M_{F606W} \gtrsim -4.8$ mag) on any GC at the location of GW170817 (Fong et al. 2019), making an in situ formation of the BNS in a GC very unlikely (only ≈0.004% of the total mass in GCs in NGC 4993 is below this limit). Progenitor formation within a GC and a later ejection before merger (e.g., Andrews & Mandel 2019) cannot be ruled out, as that would require the capability to correlate GW170817 with its parent GC after a long merger timescale.

The very old stellar population of NGC 4993 indicates long BNS merger timescales (>1 Gyr; Abbott et al. 2017c, Blanchard et al. 2017, Levan et al. 2017, Pan et al. 2017). The combination of a long inferred merger timescale and a relatively small projected offset suggests that the binary experienced a modest SN kick. Binary population synthesis modeling that used as inputs the NS mass posteriors of GW170817 derived from GW data, the measured projected offset, and the inference of the old stellar population of NGC 4993 derived a second SN kick of $\approx 300^{+250}_{-200}$ km s^{-1}, assuming that the GW170817 progenitor evolved as an isolated binary. However, observations of this single system cannot rule out the possibility of a kick fortuitously directed along the line of sight (which would minimize the projected offset) or a binary on an extended orbit that merged close to the host-galaxy center (Abbott et al. 2017c, Levan et al. 2017). Finally, the density in the merger's surroundings depends on whether the binary system has hosted a pulsar. Comparison with BNS systems in the Galaxy that are expected to merge within a Hubble time shows that in most cases the low-density cavity carved out by the pulsar winds extends to large radii that are not consistent with the early onset of the afterglow of GW170817 (Ramirez-Ruiz et al. 2019).

Until the present day, the host-galaxy demographics and the predictions from binary stellar evolution have been used to support the case of SGRBs as products of NS mergers (e.g., Berger 2014; Section 1.3). In the next decade, with a statistical sample of GW-detected BNS mergers well localized by their EM counterparts, the flow of inference can be reversed, and BNS mergers can be used to inform binary stellar evolution models (Levan et al. 2017).

8. OPEN QUESTIONS AND FUTURE PROSPECTS

8.1. Future Observations of GW170817: The Kilonova Afterglow

X-ray observations of GW170817 at $\delta t > 600$ days point to a possible flattening of the light curve (**Figure 7**). A number of factors could lead to this interesting (Hajela et al. 2021) X-ray flattening. This effect could originate from the jet dynamics (i.e., the jet hydrodynamical spreading and/or deceleration into the NR phase, an overdensity encountered by the blast wave, or possibly the emergence of an additional emission component (e.g., Granot et al. 2018b, Ryan et al. 2020). For the jet-environment parameters of GW170817 the full transition to the NR regime and the appearance of the counter jet is expected at $t_{NR} \gtrsim 3{,}000$ days, with ν_c being much greater than X-rays at the present epoch. Although the presence of an overdensity or variation in the shock microphysical parameters (e.g., p) cannot be excluded, perhaps the most interesting interpretation would be the emergence of nonthermal synchrotron emission from the deceleration of the kilonova ejecta into the environment: the kilonova afterglow (Nakar & Piran 2011, Granot et al. 2018b, Kathirgamaraju et al. 2019a, Margalit & Piran 2020).

The potential emergence of the kilonova afterglow of GW170817 in the X-rays has been discussed by Hajela et al. (2019, 2021) and Troja et al. (2020). Similar to SNe, the bulk of the kinetic energy in kilonovae is carried by slowly moving ejecta that power the UV–optical–NIR thermal emission (Section 4). The significantly lighter kilonova fastest ejecta rush ahead and shock the medium, producing synchrotron emission that is expected to peak on timescales of years. The kilonova afterglow maps the emission from this fast tail of ejecta, with $v \gtrsim 0.3c$, and constrains the ejecta kinetic energy structure in the velocity space $E_{\rm k}^{\rm KN}(\Gamma\beta)$. $E_{\rm k}^{\rm KN}(\Gamma\beta)$ carries direct information on the merger dynamics, the presence of the very fast tail of ejecta that is invoked by cocoon shock breakout models to produce GRB 170817A (Section 3.2), and, potentially, the nature of the compact object remnant (Section 8.2) (e.g., Hotokezaka et al. 2018; Radice et al. 2018a,b; Fernández et al. 2019).

Supramassive NS: a neutron star with $M_{\rm TOV} < M < M_{\rm rot}^{\rm NS}$ that will spin down through emission of GWs and light, and collapse to BH over $\sim$10–5 × 10^4 s

Stable NS: neutron star with mass below the Tolman-Oppenheimer-Volkoff (TOV) mass $M_{\rm TOV}$

Although limited statistical evidence for the emergence of a kilonova afterglow currently exist in the X-rays, the kilonova afterglow is expected to be more prominent in the radio domain because of the location of the synchrotron frequency. With the improved sensitivity of the next generation of X-ray and radio observatories (e.g., the Next Generation Very Large Array, the Square Kilometer Array phase 1-MID project, and the *Lynx X-ray Observatory*), it will be in principle possible to detect the kilonova afterglow of GW170817 for decades (Alexander et al. 2017).

8.2. Nature of the Compact-Object Remnant

GWs from the postmerger phase are the only direct probe of the nature of the merger remnant object, which might be a BH or an NS, with massive NSs above the stability thresholds imposed by the nuclear matter EoS eventually collapsing to a BH on different timescales (e.g., Fryer et al. 2015; see Bernuzzi 2020 for a recent review). A search for postmerger GWs from GW170817 on short- ($\lesssim$1 s) and intermediate-duration ($\lesssim$500 s) timescales in the kilohertz regime, where HMNS and supramassive NS[1] remnants are expected to radiate, led to no significant detection in Advanced LIGO, Advanced Virgo, and GEO600 data (Abbott et al. 2017d, 2019a). The derived limits do not constrain the direct BH collapse scenario, as the remnant BH ringdown GW signal is expected to be significantly below the threshold for current detectors (Abbott et al. 2017d). However, the postmerger GW limits interestingly lie within a factor of $\sim$10 from the theoretically predicted range of GW strain amplitudes from HMNS and supramassive NS remnants, which might be thus meaningfully probed in the future by the full LIGO-Virgo network at design sensitivity (Abbott et al. 2019a).

The nature of the merger remnant leaves several potential imprints on the EM counterpart that fall under four major categories (e.g., Bauswein et al. 2013; Metzger & Piro 2014; Margalit & Metzger 2017, 2019; Murguia-Berthier et al. 2017b; Shibata et al. 2017): (*a*) kilonova colors, (*b*) amount of ejecta mass, (*c*) ejecta kinetic energy, and (*d*) presence of a successful relativistic jet. All these signatures fundamentally depend on the lifetime of the NS remnant, with bluer, more massive, and more energetic kilonovae without a successful jet pointing to longer-lived NSs. Although EM observations of GW170817 offer no conclusive evidence, and a long-lived or stable NS cannot be entirely ruled out on EM and GW grounds (e.g., Abbott et al. 2017b, 2020b; Piro et al. 2019; Troja et al. 2020), the presence of a blue kilonova component associated with a large mass of lanthanide-free ejecta and $E_{\rm k} \sim 10^{51}$ erg (Section 4), together with a successful relativistic jet (Section 5), strongly disfavors a prompt collapse to a BH and argues in favor of an HMNS that collapsed to a BH within a second or so after merger (Granot et al. 2017, Margalit & Metzger 2017, Shibata et al. 2017, Metzger et al. 2018, Rezzolla et al. 2018, Gill et al. 2019b, Ciolfi 2020, Murguia-Berthier et al. 2021). Finally, there is no significant EM observational evidence for long-lived ($t > T_{90}$) central engine activity in the form of accretion onto a BH or spin down of a rapidly rotating NS (Abbott et al. 2017b, Pooley et al. 2018, Hajela et al. 2019; Section 5.4). EM and GW observations of GW170817 strongly motivate improvements to the high-frequency sensitivity

[1] $M_{\rm rot}^{\rm NS}$ is the mass limit for a uniformly rotating neutron star.

of GW interferometers to directly probe the outcome of the merger and accurately map EM signatures to the properties of their compact remnants.

8.3. Early Optical Observations

Owing mostly to its unfavorable sky location, AT 2017gfo was not detected in the optical until 10.9 h after the merger (Coulter et al. 2017). The emission at blue wavelengths was unexpectedly luminous for an *r*-process-powered kilonova, and several alternative models have been proposed (Section 4.4). Although the theoretical models will be refined, distinguishing between them will ultimately require high-cadence multicolor observations in the first day after a future BNS merger (e.g., Arcavi 2018). Even in a standard blue kilonova model, the shape of the light curve in the first day is a sensitive probe of the structure of the outer ejecta (Kasen et al. 2017, Banerjee et al. 2020). At sufficiently early times, additional components such as free neutron decay have been proposed to contribute to the observed emission (Kulkarni 2005, Metzger et al. 2015, Gottlieb & Loeb 2020). Polarimetry will also be a powerful tool to study the ejecta geometry, particularly in the first day or two after the merger (Section 4.5.1; Bulla et al. 2019).

8.4. Is There a Role for Other Production Sites for the *r*-Process?

The observations discussed in Section 4.3 demonstrate that GW170817 ejected about the right amount of *r*-process-enhanced material to explain Galactic nucleosynthesis if it is typical of BNS mergers (e.g., Rosswog et al. 2018). There is room for substantial future refinements in the estimates of the BNS merger rate and in the *r*-process production of individual events. Nevertheless, it is still possible that extreme or unusual SNe (e.g., Siegel et al. 2019) contribute to the observed abundances, particularly for the first *r*-process peak, where observations of metal-poor stars indicate some scatter relative to the solar abundance pattern (Sneden et al. 2008, Cowan et al. 2019). Also, emerging evidence suggests there is a substantial dispersion in the observed properties of the kilonovae associated with SGRBs (Section 4.6). Côté et al. (2019) and Ji et al. (2019) have comprehensively reviewed the connection between nucleosynthesis in NS mergers and the abundance patterns in metal-poor stars. Their reviews of the abundance ratios find a shortage of evidence that GW170817 ejected sufficient amounts of the heaviest *r*-process material relative to the lighter *r*-process. However, material with the highest $X_{\rm lan}$ might only manifest at the latest times and in the IR (Section 4.3.1). JWST and the planned 20–30-m ground-based telescopes will be necessary to obtain the required observations in the IR at late times for future NS mergers.

8.5. Neutrinos

The three most sensitive high-energy neutrino observatories (i.e., Astronomy with a Neutrino Telescope and Abyss environmental RESearch or ANTARES, the IceCube Neutrino Observatory, and the Pierre Auger Observatory) searched for GeV–EeV neutrinos associated with GW170817 and reported no evidence for directionally coincident neutrinos within ±500 s around the merger time and up to 14 days postmerger (Albert et al. 2017). A search for megaelectronvolt neutrinos with IceCube similarly led to a nondetection, consistent with the observed properties of GRB 170817A, and the expectations from SGRB jets and their extended γ-ray emission, on axis or off axis. Prompt neutrinos (i.e., neutrinos associated with the prompt GRB emission) would reveal the hadronic content of the jet and provide insight into particle acceleration and the dissipation mechanism in relativistic outflows, with the added benefit of an improved localization of the GW event (Albert et al. 2017). The detection of a long-lived source of high-energy neutrinos (timescales of approximately days) would additionally point to an equally long-lived or indefinitely stable millisecond magnetar merger remnant (e.g., Fang & Metzger 2017).

8.6. Searches for Kilonovae Untriggered by Gravitational Wave or Gamma-Ray Burst Detections

Blind searches for kilonovae as optical transients untriggered by SGRBs or GWs have been carried out before and after the discovery of AT 2017gfo using data streams from a variety of telescope surveys (Doctor et al. 2017, Kasliwal et al. 2017b, Smartt et al. 2017, Yang et al. 2017, Andreoni et al. 2020, McBrien et al. 2020). No kilonova has been confidently identified so far, with only one potential candidate reported by McBrien et al. (2020). However, the null results from these searches can be used to independently constrain the rate of kilonovae in the local Universe. The tightest limit on the rate of kilonovae with luminosity similar to AT 2017gfo is $\mathcal{R} < 800\,\mathrm{Gpc}^{-3}\,\mathrm{year}^{-1}$ (Kasliwal et al. 2017b; also see Andreoni et al. 2020, their figure 9). A direct comparison to the rates of SGRBs and BNS mergers derived from GWs of **Figure 3** might not be justified, as we have clear evidence of kilonovae that are fainter than AT 2017gfo (Section 4.6). The major challenges faced by all of these attempts stem from the combination of the intrinsically low rate and faintness of the expected kilonova events, the limited volume of the Universe probed, and the comparatively large rate of contaminants. Increasing the depth of these searches is mandatory to reveal the population of jet-less BNS mergers (if there), which might go undetected in the absence of a GW trigger.

9. CONCLUSIONS

The first joint detection of GWs and light from the same celestial body offered an unprecedented opportunity for advancement in astrophysics, fundamental physics, gravitation, and cosmology. Like few other astronomical events, GW170817 and its EM counterparts tied together many threads of previous inquiry. The thousands of scientists that participated in the enormous collective observational endeavor demonstrated a litany of firsts:

- First GW detection of a BNS merger
- First secure discovery of an EM counterpart to a GW source
- First observations of a structured relativistic jet seen from the side
- First definitive detection of a kilonova
- First optical–NIR spectroscopy of a kilonova
- First BNS merger to be localized in the local Universe

The interpretation of the observations relied on decades of theoretical work, with many of the key advances occurring only in the last few years before GW170817. That the observations were so readily interpretable within this framework represents a triumph of theoretical astrophysics.

The implications of these studies of GW170817 bridge multiple disciplines:

- The properties of GW170817, GRB 170817A, and the nonthermal afterglow provide the first direct connection between SGRBs and BNS mergers. GW170817 demonstrated that BNS mergers can successfully launch highly collimated ultrarelativistic jets with core properties similar to those of SGRBs and substantial angular and radial structure that was simply impossible to probe before this event. GW170817 provided the first opportunity to appreciate that such a structure exists and has observable consequences.
- Photometric and spectroscopic observations of AT 2017gfo in the optical and IR wavelengths established that BNS mergers are cosmic sites of *r*-process nucleosynthesis, thus identifying the origin of (at least some of) the heaviest chemical elements of the periodic table.

- The small interval of time between the GW coalescence and the detection of γ-rays enabled new tests of GR and fundamental physics, which, among other results, led to severe constraints on a sizeable fraction of the parameter space of modified theories of gravity.
- GW measurements enabled direct constraints on the EoS of dense nuclear matter, which were strengthened by the combination with information from the EM counterpart. This multimessenger approach will be a major emphasis of future BNS investigations.
- Standard-siren-based measurements of H_0 from EM-localized GW sources like GW170817 provide a novel method of inference in cosmology. This method, put into practice with GW170817 for the first time, allows a measurement of H_0 in the local Universe that does not rely on a cosmic distance ladder, and it is thus well positioned as one of the most promising venues to solve the current H_0 tension.

Against this backdrop of progress, GW170817 and its EM counterparts left key questions unanswered: (*a*) GWs: What is the EoS of dense nuclear matter? What is the ultimate merger remnant? (*b*) Kilonovae: What is the origin of the blue emission component? Are BNS mergers the only significant site for the *r*-process? (*c*) Jets: Do all BNS mergers successfully launch ultrarelativistic jets into their environments? Is there a population of SGRBs powered by NS–BH mergers? Does jet launching require collapse to a BH?

This comprehensive data set on GW170817 is unlikely to be equaled for any BNS merger in the near future. A critical question for future work is assessing how typical this event was of the whole population. There are hints from observations of SGRBs (Section 4.6) that the associated kilonovae exhibit substantial dispersion. The future of the field also relies on improved multidimensional radiative transfer modeling, which is necessary to more quantitatively constrain nucleosynthesis and ejecta parameters in kilonovae, and improved MHD simulations of jets with realistic structures.

Looking ahead, the increased sensitivity of future GW observatories will allow us to probe more distant populations of GW sources. However, GW interferometers are sensitive to the gravitational strain h, which scales as $1/D_{\rm L}$ (where $D_{\rm L}$ is the distance to a source), whereas optical telescopes are sensitive to the energy flux, which scales as $1/D_{\rm L}^2$. The ultimate design sensitivity of Advanced LIGO will be sensitive to BNS systems out to ∼200 Mpc (and NS–BH star mergers at several hundred megaparsecs), and the proposed A+ upgrades by the 2025 time frame will aim to increase the sensitivity by an additional factor of about 2. Therefore, planned technology developments in GW interferometers will rapidly start producing detections at distances where the expected optical KN counterparts are exceedingly dim, stretching the capabilities of even JWST and the next-generation Extremely Large Telescopes, and definitely beyond the reach of current X-ray, radio, and γ-ray facilities. For multimessenger astrophysics with GWs to flourish and keep its scientific promise, it is mandatory to match the upcoming generation of GW detectors with a new generation of more sensitive EM observatories across the spectrum.

DISCLOSURE STATEMENT

The authors are not aware of any affiliations, memberships, funding, or financial holdings that might be perceived as affecting the objectivity of this review.

ACKNOWLEDGMENTS

We are grateful to the numerous observatory staffs around the globe who enabled the unprecedented observational campaign on this historic object. The literature on this subject extends to thousands of publications, and we apologize in advance to those colleagues whose work we could not adequately discuss here. We thank our long-time collaborators, including Edo Berger and Wen-fai Fong, for fruitful observational campaigns over the years and acknowledge the key role that discussion and models produced by Brian Metzger and Dan Kasen had in enabling our interpretation of the data. It is our pleasure to acknowledge K.D. Alexander, D.A. Brown, P.K. Blanchard, L. DeMarchi, M.R. Drout, D. Finstad, G. Ghirlanda, O. Gottlieb, J. Granot, K. Hotokezaka, A. Kathirgamaraju, D. Lazzati, B. Margalit, S. Rosswog, and V.A. Villar for their comments and for promptly replying to our requests and sharing data and results from simulations that have been used in figures of this review. This research was supported in part by the National Science Foundation under grants NSF PHY-1748958, AST-1909796, and AST-1944985. Portions of this work were initiated at the program on "The New Era of Gravitational-Wave Physics and Astrophysics" (GRAVAST19) at the Kavli Institute for Theoretical Physics, UC Santa Barbara. R.M. acknowledges partial support from NASA through Chandra Award Number G09-20058A and through Space Telescope Science Institute program #15606. R.C. acknowledges partial support from Chandra grants DD8-19101B and GO9-20058B.

LITERATURE CITED

Aasi J, Abadie J, Abbott BP, Abbott R, Abbott T, et al. 2015. *Class. Quantum Gravity* 32:115012
Abbott BP, Abbott R, Abbott TD, et al. 2016. *Phys. Rev. Lett.* 116:061102
Abbott BP, Abbott R, Abbott TD, et al. 2017a. *Ap. J. Lett.* 848:L12
Abbott BP, Abbott R, Abbott TD, et al. 2017b. *Ap. J. Lett.* 848:L13
Abbott BP, Abbott R, Abbott TD, et al. 2017c. *Ap. J. Lett.* 850:L40
Abbott BP, Abbott R, Abbott TD, et al. 2017d. *Ap. J. Lett.* 851:L16
Abbott BP, Abbott R, Abbott TD, et al. 2017e. *Nature* 551:85–88
Abbott BP, Abbott R, Abbott TD, et al. 2017f. *Phys. Rev. Lett.* 119:161101
Abbott BP, Abbott R, Abbott TD, et al. 2018. *Phys. Rev. Lett.* 121:161101
Abbott BP, Abbott R, Abbott TD, et al. 2019a. *Phys. Rev. X* 9:011001
Abbott BP, Abbott R, Abbott TD, et al. 2019b. *Phys. Rev. Lett.* 123:011102
Abbott BP, Abbott R, Abbott TD, et al. 2020a. *Ap. J. Lett.* 892:L3
Abbott BP, Abbott R, Abbott TD, et al. 2020b. *Class. Quantum Gravity* 37:045006
Acernese F, Agathos M, Agatsuma K, et al. 2015. *Class. Quantum Gravity* 32:024001
Albert A, André M, Anghinolfi M, et al. 2017. *Ap. J. Lett.* 850:L35
Alexander KD, Berger E, Fong W, et al. 2017. *Ap. J. Lett.* 848:L21
Alexander KD, Margutti R, Blanchard PK, et al. 2018. *Ap. J. Lett.* 863:L18
Aloy MA, Janka HT, Müller E. 2005. *Astron. Astrophys.* 436:273–311
Andreoni I, Ackley K, Cooke J, et al. 2017. *Publ. Astron. Soc. Aust.* 34:e069
Andreoni I, Kool EC, Sagúes Carracedo A, et al. 2020. *Ap. J.* 904:155
Andrews JJ, Mandel I. 2019. *Ap. J. Lett.* 880:L8
Antoniadis J, Freire PCC, Wex N, et al. 2013. *Science* 340:1233232
Arcavi I. 2018. *Ap. J. Lett.* 855:L23
Arcavi I, Hosseinzadeh G, Howell DA, et al. 2017. *Nature* 551:64–66
Arnett WD. 1982. *Ap. J.* 253:785–97
Ascenzi S, Coughlin MW, Dietrich T, et al. 2019. *MNRAS* 486:672–90
Baker T, Bellini E, Ferreira PG, et al. 2017. *Phys. Rev. Lett.* 119:251301
Banerjee S, Tanaka M, Kawaguchi K, Kato D, Gaigalas G. 2020. *Ap. J.* 901:29
Barnes J, Kasen D. 2013. *Ap. J.* 775:18
Barnes J, Kasen D, Wu MR, Martínez-Pinedo G. 2016. *Ap. J.* 829:110
Bauswein A, Goriely S, Janka HT. 2013. *Ap. J.* 773:78
Bauswein A, Just O, Janka HT, Stergioulas N. 2017. *Ap. J. Lett.* 850:L34
Beniamini P, Duran RB, Petropoulou M, Giannios D. 2020a. *Ap. J. Lett.* 895:L33
Beniamini P, Granot J, Gill R. 2020b. *MNRAS* 493:3521–34

Beniamini P, Petropoulou M, Barniol Duran R, Giannios D. 2019. *MNRAS* 483:840–51
Berger E. 2014. *Annu. Rev. Astron. Astrophys.* 52:43–105
Berger E, Fong W, Chornock R. 2013. *Ap. J. Lett.* 774:L23
Bernuzzi S. 2020. *Gen. Relativ. Gravit.* 52:108
Blanchard PK, Berger E, Fong W, et al. 2017. *Ap. J. Lett.* 848:L22
Boran S, Desai S, Kahya EO, Woodard RP. 2018. *Phys. Rev. D* 97:041501
Bromberg O, Nakar E, Piran T, Sari R. 2011. *Ap. J.* 740:100
Bromberg O, Tchekhovskoy A, Gottlieb O, Nakar E, Piran T. 2018. *MNRAS* 475:2971–77
Bulla M, Covino S, Kyutoku K, et al. 2019. *Nat. Astron.* 3:99–106
Burbidge EM, Burbidge GR, Fowler WA, Hoyle F. 1957. *Rev. Mod. Phys.* 29:547–650
Burns E. 2020. *Living Rev. Relativ.* 23:4
Burns E, Veres P, Connaughton V, et al. 2018. *Ap. J. Lett.* 863:L34
Burrows DN, Grupe D, Capalbi M, et al. 2006. *Ap. J.* 653:468–73
Cameron AGW. 1957. *Publ. Astron. Soc. Pac.* 69:201–22
Capano CD, Tews I, Brown SM, et al. 2020. *Nat. Astron.* 4:625–32
Cantiello M, Jensen JB, Blakeslee JP, et al. 2018. *Ap. J. Lett.* 854:L31
Chen HY, Fishbach M, Holz DE. 2018. *Nature* 562:310–11
Chen HY, Vitale S, Narayan R. 2019. *Phys. Rev. X* 9:031028
Chornock R, Berger E, Kasen D, et al. 2017. *Ap. J. Lett.* 848:L19
Ciolfi R. 2020. *MNRAS* 495:L66–70
Corsi A, Hallinan GW, Lazzati D, et al. 2018. *Ap. J. Lett.* 861:L10
Côté B, Eichler M, Arcones A, et al. 2019. *Ap. J.* 875:106
Coughlin MW, Dietrich T. 2019. *Phys. Rev. D* 100:043011
Coughlin MW, Dietrich T, Doctor Z, et al. 2018. *MNRAS* 480:3871–78
Coughlin MW, Dietrich T, Margalit B, Metzger BD. 2019. *MNRAS* 489:L91–96
Coulter DA, Foley RJ, Kilpatrick CD, et al. 2017. *Science* 358:1556–58
Covino S, Wiersema K, Fan YZ, et al. 2017. *Nat. Astron.* 1:791–94
Cowan JJ, Sneden C, Lawler JE, et al. 2021. *Rev. Mod. Phys.* 93:015002
Cowperthwaite PS, Berger E, Villar VA, et al. 2017. *Ap. J. Lett.* 848:L17
Creminelli P, Vernizzi F. 2017. *Phys. Rev. Lett.* 119:251302
D'Avanzo P, Campana S, Salafia OS, et al. 2018. *Astron. Astrophys.* 613:L1
De S, Finstad D, Lattimer JM, et al. 2018a. *Phys. Rev. Lett.* 121:091102
De S, Finstad D, Lattimer JM, et al. 2018b. *Phys. Rev. Lett.* 121:259902
de Rham C, Melville S. 2018. *Phys. Rev. Lett.* 121:221101
Dessart L, Ott CD, Burrows A, Rosswog S, Livne E. 2009. *Ap. J.* 690:1681–705
Díaz MC, Macri LM, Garcia Lambas D, et al. 2017. *Ap. J. Lett.* 848:L29
Dima A, Vernizzi F. 2018. *Phys. Rev. D* 97:101302
Dobie D, Kaplan DL, Murphy T, et al. 2018. *Ap. J. Lett.* 858:L15
Doctor Z, Kessler R, Chen HY, et al. 2017. *Ap. J.* 837:57
Drout MR, Piro AL, Shappee BJ, et al. 2017. *Science* 358:1570–74
Duffell PC, Quataert E, Kasen D, Klion H. 2018. *Ap. J.* 866:3
Duffell PC, Quataert E, MacFadyen AI. 2015. *Ap. J.* 813:64
Eastman RG, Pinto PA. 1993. *Ap. J.* 412:731–51
Eichler D, Livio M, Piran T, Schramm DN. 1989. *Nature* 340:126–28
Evans PA, Beardmore AP, Page KL, et al. 2009. *MNRAS* 397:1177–201
Evans PA, Cenko SB, Kennea JA, et al. 2017. *Science* 358:1565–70
Ezquiaga JM, Zumalacárregui M. 2017. *Phys. Rev. Lett.* 119:251304
Fahlman S, Fernández R. 2018. *Ap. J. Lett.* 869:L3
Fang K, Metzger BD. 2017. *Ap. J.* 849:153
Feeney SM, Peiris HV, Williamson AR, et al. 2019. *Phys. Rev. Lett.* 122:061105
Fernández R, Metzger BD. 2016. *Annu. Rev. Nucl. Part. Sci.* 66:23–45
Fernández R, Tchekhovskoy A, Quataert E, Foucart F, Kasen D. 2019. *MNRAS* 482:3373–93

Finstad D, De S, Brown DA, Berger E, Biwer CM. 2018. *Ap. J. Lett.* 860:L2
Fong W, Berger E, Blanchard PK, et al. 2017. *Ap. J. Lett.* 848:L23
Fong W, Berger E, Margutti R, Zauderer BA. 2015. *Ap. J.* 815:102
Fong W, Berger E, Metzger BD, et al. 2014. *Ap. J.* 780:118
Fong W, Blanchard PK, Alexander KD, et al. 2019. *Ap. J. Lett.* 883:L1
Fong W, Laskar T, Rastinejad J, et al. 2021. *Ap. J.* 906:127
Fontes CJ, Fryer CL, Hungerford AL, Wollaeger RT, Korobkin O. 2020. *MNRAS* 493:4143–71
Fontes CJ, Fryer CL, Hungerford AL, et al. 2017. arXiv:1702.02990
Fraija N, De Colle F, Veres P, et al. 2019. *Ap. J.* 871:123
Frebel A. 2018. *Annu. Rev. Nucl. Part. Sci.* 68:237–69
Freiburghaus C, Rosswog S, Thielemann FK. 1999. *Ap. J. Lett.* 525:L121–24
Fryer CL, Belczynski K, Ramirez-Ruiz E, et al. 2015. *Ap. J.* 812:24
Gall C, Hjorth J, Rosswog S, Tanvir NR, Levan AJ. 2017. *Ap. J. Lett.* 849:L19
Geng JJ, Zhang B, Kölligan A, Kuiper R, Huang YF. 2019. *Ap. J. Lett.* 877:L40
Ghirlanda G, Salafia OS, Paragi Z, et al. 2019. *Science* 363:968–71
Ghirlanda G, Salafia OS, Pescalli A, et al. 2016. *Astron. Astrophys.* 594:A84
Gill R, Granot J. 2018. *MNRAS* 478:4128–41
Gill R, Granot J. 2020. *MNRAS* 491:5815–25
Gill R, Granot J, De Colle F, Urrutia G. 2019a. *Ap. J.* 883:15
Gill R, Nathanail A, Rezzolla L. 2019b. *Ap. J.* 876:139
Goldstein A, Veres P, Burns E, et al. 2017. *Ap. J. Lett.* 848:L14
Gompertz BP, Levan AJ, Tanvir NR, et al. 2018. *Ap. J.* 860:62
Goriely S, Bauswein A, Janka HT. 2011. *Ap. J. Lett.* 738:L32
Gottlieb O, Loeb A. 2020. *MNRAS* 493:1753–60
Gottlieb O, Nakar E, Bromberg O. 2021. *MNRAS* 500:3511–26
Gottlieb O, Nakar E, Piran T. 2018a. *MNRAS* 473:576–84
Gottlieb O, Nakar E, Piran T. 2019. *MNRAS* 488:2405–11
Gottlieb O, Nakar E, Piran T, Hotokezaka K. 2018b. *MNRAS* 479:588–600
Granot J, De Colle F, Ramirez-Ruiz E. 2018a. *MNRAS* 481:2711–20
Granot J, Gill R, Guetta D, De Colle F. 2018b. *MNRAS* 481:1597–608
Granot J, Guetta D, Gill R. 2017. *Ap. J. Lett.* 850:L24
Grossman D, Korobkin O, Rosswog S, Piran T. 2014. *MNRAS* 439:757–70
Grupe D, Burrows DN, Patel SK, et al. 2006. *Ap. J.* 653:462–67
Guidorzi C, Margutti R, Brout D, et al. 2017. *Ap. J. Lett.* 851:L36
Haggard D, Nynka M, Ruan JJ, et al. 2017. *Ap. J. Lett.* 848:L25
Hajela A, Margutti R, Alexander KD, et al. 2019. *Ap. J. Lett.* 886:L17
Hajela A, Margutti R, Bright J, et al. 2021. GRB Coord. Netw., Circ. Serv. No. 29375
Hallinan G, Corsi A, Mooley KP, et al. 2017. *Science* 358:1579–83
Hinderer T, Nissanke S, Foucart F, et al. 2019. *Phys. Rev. D* 100:063021
Hjorth J, Levan AJ, Tanvir NR, et al. 2017. *Ap. J. Lett.* 848:L31
Holmbeck EM, Hansen TT, Beers TC, et al. 2020. *Ap. J. Suppl.* 249:30
Holmbeck EM, Sprouse TM, Mumpower MR, et al. 2019. *Ap. J.* 870:23
Holz DE, Hughes SA. 2005. *Ap. J.* 629:15–22
Horowitz CJ, Arcones A, Côté B, et al. 2019. *J. Phys. G Nuclear Phys.* 46:083001
Hotokezaka K, Kiuchi K, Kyutoku K, et al. 2013. *Phys. Rev. D* 87:024001
Hotokezaka K, Kiuchi K, Shibata M, Nakar E, Piran T. 2018. *Ap. J.* 867:95
Hotokezaka K, Nakar E. 2020. *Ap. J.* 891:152
Hotokezaka K, Nakar E, Gottlieb O, et al. 2019. *Nat. Astron.* 3:940–44
Hotokezaka K, Piran T, Paul M. 2015. *Nat. Phys.* 11:1042
Hu L, Wu X, Andreoni I, et al. 2017. *Sci. Bull.* 62:1433–38
Hulse RA, Taylor JH. 1975. *Ap. J. Lett.* 195:L51–53
Im M, Yoon Y, Lee SKJ, et al. 2017. *Ap. J. Lett.* 849:L16

Ioka K, Nakamura T. 2019. *MNRAS* 487:4884–89
Ji AP, Drout MR, Hansen TT. 2019. *Ap. J.* 882:40
Ji AP, Frebel A, Chiti A, Simon JD. 2016. *Nature* 531:610–13
Jin ZP, Covino S, Liao NH, et al. 2020. *Nat. Astron.* 4:77–82
Jin ZP, Hotokezaka K, Li X, et al. 2016. *Nat. Commun.* 7:12898
Just O, Bauswein A, Ardevol Pulpillo R, Goriely S, Janka HT. 2015. *MNRAS* 448:541–67
Karp AH, Lasher G, Chan KL, Salpeter EE. 1977. *Ap. J.* 214:161–78
Kasen D, Badnell NR, Barnes J. 2013. *Ap. J.* 774:25
Kasen D, Barnes J. 2019. *Ap. J.* 876:128
Kasen D, Fernández R, Metzger BD. 2015. *MNRAS* 450:1777–86
Kasen D, Metzger B, Barnes J, Quataert E, Ramirez-Ruiz E. 2017. *Nature* 551:80–84
Kasliwal MM, Anand S, Ahumada T, et al. 2020. *Ap. J.* 905:145
Kasliwal MM, Kasen D, Lau RM, et al. 2019. *MNRAS Lett.* 2019:slz007
Kasliwal MM, Korobkin O, Lau RM, Wollaeger R, Fryer CL. 2017a. *Ap. J. Lett.* 843:L34
Kasliwal MM, Nakar E, Singer LP, et al. 2017b. *Science* 358:1559–65
Kathirgamaraju A, Giannios D, Beniamini P. 2019a. *MNRAS* 487:3914–21
Kathirgamaraju A, Tchekhovskoy A, Giannios D, Barniol Duran R. 2019b. *MNRAS* 484:L98–103
Kawaguchi K, Shibata M, Tanaka M. 2018. *Ap. J. Lett.* 865:L21
Kawaguchi K, Shibata M, Tanaka M. 2020. *Ap. J.* 889:171
Kilpatrick CD, Foley RJ, Kasen D, et al. 2017. *Science* 358:1583–87
Kim S, Schulze S, Resmi L, et al. 2017. *Ap. J. Lett.* 850:L21
Kisaka S, Ioka K, Nakar E. 2016. *Ap. J.* 818:104
Kiuchi K, Kyutoku K, Shibata M, Taniguchi K. 2019. *Ap. J. Lett.* 876:L31
Kiziltan B, Kottas A, De Yoreo M, Thorsett SE. 2013. *Ap. J.* 778:66
Klebesadel RW, Strong IB, Olson RA. 1973. *Ap. J. Lett.* 182:L85–88
Korobkin O, Rosswog S, Arcones A, Winteler C. 2012. *MNRAS* 426:1940–49
Korobkin O, Wollaeger RT, Fryer CL, et al. 2021. *Ap. J.* 910:116
Kouveliotou C, Meegan CA, Fishman GJ, et al. 1993. *Ap. J. Lett.* 413:L101–4
Kulkarni SR. 2005. arXiv:astro–ph/0510256
Kyutoku K, Ioka K, Shibata M. 2014. *MNRAS* 437:L6–10
Lamb GP, Kobayashi S. 2018. *MNRAS* 478:733–40
Lamb GP, Lyman JD, Levan AJ, et al. 2019a. *Ap. J. Lett.* 870:L15
Lamb GP, Mandel I, Resmi L. 2018. *MNRAS* 481:2581–89
Lamb GP, Tanvir NR, Levan AJ, et al. 2019b. *Ap. J.* 883:48
Langlois D, Saito R, Yamauchi D, Noui K. 2018. *Phys. Rev. D* 97:061501
Lattimer JM, Schramm DN. 1974. *Ap. J. Lett.* 192:L145–47
Lattimer JM, Schramm DN. 1976. *Ap. J.* 210:549–67
Lazzati D, Deich A, Morsony BJ, Workman JC. 2017a. *MNRAS* 471:1652–61
Lazzati D, López-Cámara D, Cantiello M, et al. 2017b. *Ap. J. Lett.* 848:L6
Lazzati D, Perna R. 2019. *Ap. J.* 881:89
Lazzati D, Perna R, Morsony BJ, et al. 2018. *Phys. Rev. Lett.* 120:241103
Leibler CN, Berger E. 2010. *Ap. J.* 725:1202–14
Levan AJ, Lyman JD, Tanvir NR, et al. 2017. *Ap. J. Lett.* 848:L28
Li LX, Paczyński B. 1998. *Ap. J. Lett.* 507:L59–62
Lippuner J, Roberts LF. 2015. *Ap. J.* 815:82
Lipunov VM, Gorbovskoy E, Kornilov VG, et al. 2017. *Ap. J. Lett.* 850:L1
Lyman JD, Lamb GP, Levan AJ, et al. 2018. *Nat. Astron.* 2:751–54
Makhathini S, Mooley KP, Brightman M, et al. 2020. *Ap. J.* Submitted. arXiv:2006.02382
Mandel I. 2018. *Ap. J. Lett.* 853:L12
Margalit B, Metzger BD. 2017. *Ap. J. Lett.* 850:L19
Margalit B, Metzger BD. 2019. *Ap. J. Lett.* 880:L15
Margalit B, Piran T. 2020. *MNRAS* 495:4981–93

Margutti R, Alexander KD, Xie X, et al. 2018. *Ap. J. Lett.* 856:L18
Margutti R, Berger E, Fong W, et al. 2017. *Ap. J. Lett.* 848:L20
Margutti R, Chincarini G, Granot J, et al. 2011. *MNRAS* 417:2144–60
Matsumoto T, Nakar E, Piran T. 2019. *MNRAS* 483:1247–55
McBrien OR, Smartt SJ, Huber ME, et al. 2021. *MNRAS* 500:4213–28
McCully C, Hiramatsu D, Howell DA, et al. 2017. *Ap. J. Lett.* 848:L32
Meng YZ, Geng JJ, Zhang BB, et al. 2018. *Ap. J.* 860:72
Metzger BD. 2019. *Living Rev. Relativ.* 23:1–89
Metzger BD, Bauswein A, Goriely S, Kasen D. 2015. *MNRAS* 446:1115–20
Metzger BD, Berger E. 2012. *Ap. J.* 746:48
Metzger BD, Fernández R. 2014. *MNRAS* 441:3444–53
Metzger BD, Martínez-Pinedo G, Darbha S, et al. 2010. *MNRAS* 406:2650–62
Metzger BD, Piro AL. 2014. *MNRAS* 439:3916–30
Metzger BD, Quataert E, Thompson TA. 2008. *MNRAS* 385:1455–60
Metzger BD, Thompson TA, Quataert E. 2018. *Ap. J.* 856:101
Moharana R, Piran T. 2017. *MNRAS* 472:L55–59
Mooley KP, Deller AT, Gottlieb O, et al. 2018a. *Nature* 561:355–59
Mooley KP, Frail DA, Dobie D, et al. 2018b. *Ap. J. Lett.* 868:L11
Most ER, Weih LR, Rezzolla L, Schaffner-Bielich J. 2018. *Phys. Rev. Lett.* 120:251103
Mumpower MR, Surman R, McLaughlin GC, Aprahamian A. 2016. *Prog. Part. Nuclear Phys.* 86:86–126
Murguia-Berthier A, Ramirez-Ruiz E, De Colle F, et al. 2021. *Ap. J.* 908:152
Murguia-Berthier A, Ramirez-Ruiz E, Kilpatrick CD, et al. 2017a. *Ap. J. Lett.* 848:L34
Murguia-Berthier A, Ramirez-Ruiz E, Montes G, et al. 2017b. *Ap. J. Lett.* 835:L34
Nagakura H, Hotokezaka K, Sekiguchi Y, Shibata M, Ioka K. 2014. *Ap. J. Lett.* 784:L28
Nakar E. 2020. *Phys. Rep.* 886:1–84
Nakar E, Gottlieb O, Piran T, Kasliwal MM, Hallinan G. 2018. *Ap. J.* 867:18
Nakar E, Piran T. 2011. *Nature* 478:82–84
Nakar E, Piran T. 2017. *Ap. J.* 834:28
Nakar E, Piran T. 2018. *MNRAS* 478:407–15
Nakar E, Piran T. 2021. *Ap. J.* 909:114
Narayan R, Paczynski B, Piran T. 1992. *Ap. J. Lett.* 395:L83–86
Nicholl M, Berger E, Kasen D, et al. 2017. *Ap. J. Lett.* 848:L18
Nissanke S, Holz DE, Dalal N, et al. 2013. arXiv:1307.2638 [astro-ph]
Nissanke S, Holz DE, Hughes SA, Dalal N, Sievers JL. 2010. *Ap. J.* 725:496–514
Nugent AE, Fong WF, Dong Y, et al. 2020. *Ap. J.* 904:52
Nynka M, Ruan JJ, Haggard D, Evans PA. 2018. *Ap. J. Lett.* 862:L19
Oechslin R, Janka HT, Marek A. 2007. *Astron. Astrophys.* 467:395–409
Paczynski B. 1986. *Ap. J. Lett.* 308:L43–46
Palmese A, Hartley W, Tarsitano F, et al. 2017. *Ap. J. Lett.* 849:L34
Pan YC, Kilpatrick CD, Simon JD, et al. 2017. *Ap. J. Lett.* 848:L30
Pardo K, Fishbach M, Holz DE, Spergel DN. 2018. *J. Cosmol. Astropart. Phys.* 2018:048
Perego A, Radice D, Bernuzzi S. 2017. *Ap. J. Lett.* 850:L37
Perego A, Rosswog S, Cabezón RM, et al. 2014. *MNRAS* 443:3134–56
Pian E, D'Avanzo P, Benetti S, et al. 2017. *Nature* 551:67–70
Piro AL, Kollmeier JA. 2018. *Ap. J.* 855:103
Piro L, Troja E, Zhang B, et al. 2019. *MNRAS* 483:1912–21
Planck Collab., Ade PAR, Aghanim N, et al. 2016. *Astron. Astrophys.* 594:A13
Pol N, McLaughlin M, Lorimer DR. 2020. *Res. Notes Am. Astron. Soc.* 4:22
Pooley D, Kumar P, Wheeler JC, Grossan B. 2018. *Ap. J. Lett.* 859:L23
Pozanenko AS, Barkov MV, Minaev PY, et al. 2018. *Ap. J. Lett.* 852:L30
Qian YZ, Wasserburg GJ. 2007. *Phys. Rep.* 442:237–68
Qian YZ, Woosley SE. 1996. *Ap. J.* 471:331–51

Radice D, Bernuzzi S, Perego A. 2020. *Annu. Rev. Nucl. Part. Sci.* 70:95–119
Radice D, Dai L. 2019. *Eur. Phys. J. A* 55:50
Radice D, Perego A, Hotokezaka K, et al. 2018a. *Ap. J.* 869:130
Radice D, Perego A, Hotokezaka K, et al. 2018b. *Ap. J. Lett.* 869:L35
Radice D, Perego A, Zappa F, Bernuzzi S. 2018c. *Ap. J. Lett.* 852:L29
Ramirez-Ruiz E, Andrews JJ, Schrøder SL. 2019. *Ap. J. Lett.* 883:L6
Ramirez-Ruiz E, Celotti A, Rees MJ. 2002. *MNRAS* 337:1349–56
Resmi L, Schulze S, Ishwara-Chandra CH, et al. 2018. *Ap. J.* 867:57
Rezzolla L, Most ER, Weih LR. 2018. *Ap. J. Lett.* 852:L25
Riess AG, Casertano S, Yuan W, Macri LM, Scolnic D. 2019. *Ap. J.* 876:85
Riess AG, Macri LM, Hoffmann SL, et al. 2016. *Ap. J.* 826:56
Roberts LF, Kasen D, Lee WH, Ramirez-Ruiz E. 2011. *Ap. J. Lett.* 736:L21
Roederer IU, Hattori K, Valluri M. 2018. *Astron. J.* 156:179
Rossi A, Stratta G, Maiorano E, et al. 2020. *MNRAS* 493:3379–97
Rosswog S, Feindt U, Korobkin O, et al. 2017. *Class. Quantum Gravity* 34:104001
Rosswog S, Korobkin O, Arcones A, Thielemann FK, Piran T. 2014. *MNRAS* 439:744–56
Rosswog S, Liebendörfer M, Thielemann FK, et al. 1999. *Astron. Astrophys.* 341:499–526
Rosswog S, Sollerman J, Feindt U, et al. 2018. *Astron. Astrophys.* 615:A132
Ruan JJ, Nynka M, Haggard D, Kalogera V, Evans P. 2018. *Ap. J. Lett.* 853:L4
Ruiz M, Shapiro SL, Tsokaros A. 2018. *Phys. Rev. D* 97:021501
Ryan G, van Eerten H, Piro L, Troja E. 2020. *Ap. J.* 896:166
Sakstein J, Jain B. 2017. *Phys. Rev. Lett.* 119:251303
Salafia OS, Ghirlanda G, Ascenzi S, Ghisellini G. 2019. *Astron. Astrophys.* 628:A18
Salafia OS, Ghisellini G, Ghirlanda G, Colpi M. 2018. *Astron. Astrophys.* 619:A18
Salafia OS, Giacomazzo B. 2021. *Astron. Astrophys.* 645:A93
Sari R, Piran T, Narayan R. 1998. *Ap. J. Lett.* 497:L17–20
Savchenko V, Ferrigno C, Kuulkers E, et al. 2017. *Ap. J. Lett.* 848:L15
Schlafly EF, Finkbeiner DP. 2011. *Ap. J.* 737:103
Schutz BF. 1986. *Nature* 323:310–11
Schutz BF. 2011. *Class. Quantum Gravity* 28:125023
Sekiguchi Y, Kiuchi K, Kyutoku K, Shibata M, Taniguchi K. 2016. *Phys. Rev. D* 93:124046
Shappee BJ, Simon JD, Drout MR, et al. 2017. *Science* 358:1574–78
Shen S, Cooke RJ, Ramirez-Ruiz E, et al. 2015. *Ap. J.* 807:115
Shibata M, Fujibayashi S, Hotokezaka K, et al. 2017. *Phys. Rev. D* 96:123012
Shibata M, Hotokezaka K. 2019. *Annu. Rev. Nucl. Part. Sci.* 69:41–64
Shibata M, Zhou E, Kiuchi K, Fujibayashi S. 2019. *Phys. Rev. D* 100:023015
Shoemaker IM, Murase K. 2018. *Phys. Rev. D* 97:083013
Siebert MR, Foley RJ, Drout MR, et al. 2017. *Ap. J. Lett.* 848:L26
Siegel DM, Barnes J, Metzger BD. 2019. *Nature* 569:241–44
Siegel DM, Ciolfi R, Rezzolla L. 2014. *Ap. J. Lett.* 785:L6
Sironi L, Spitkovsky A, Arons J. 2013. *Ap. J.* 771:54
Smartt SJ, Chen TW, Jerkstrand A, et al. 2017. *Nature* 551:75–79
Sneden C, Cowan JJ, Gallino R. 2008. *Annu. Rev. Astron. Astrophys.* 46:241–88
Soares-Santos M, Holz DE, Annis J, et al. 2017. *Ap. J. Lett.* 848:L16
Suess HE, Urey HC. 1956. *Rev. Mod. Phys.* 28:53–74
Sugita S, Kawai N, Nakahira S, et al. 2018. *Publ. Astron. Soc. Jpn.* 70:81
Sun H, Zhang B, Li Z. 2015. *Ap. J.* 812:33
Symbalisty E, Schramm DN. 1982. *Ap. Lett.* 22:143–45
Tanaka M, Hotokezaka K. 2013. *Ap. J.* 775:113
Tanaka M, Kato D, Gaigalas G, Kawaguchi K. 2020. *MNRAS* 496:1369–92
Tanaka M, Kato D, Gaigalas G, et al. 2018. *Ap. J.* 852:109
Tanaka M, Utsumi Y, Mazzali PA, et al. 2017. *Publ. Astron. Soc. Jpn.* 69:102

Tanvir NR, Levan AJ, Fruchter AS, et al. 2013. *Nature* 500:547–49
Tanvir NR, Levan AJ, González-Fernández C, et al. 2017. *Ap. J. Lett.* 848:L27
Taylor JH, Weisberg JM. 1982. *Ap. J.* 253:908–20
Troja E, Castro-Tirado AJ, Becerra González J, et al. 2019a. *MNRAS* 489:2104–16
Troja E, Piro L, Ryan G, et al. 2018a. *MNRAS* 478:L18–23
Troja E, Piro L, van Eerten H, et al. 2017. *Nature* 551:71–74
Troja E, Ryan G, Piro L, et al. 2018b. *Nat. Commun.* 9:4089
Troja E, Sakamoto T, Cenko SB, et al. 2016. *Ap. J.* 827:102
Troja E, van Eerten H, Ryan G, et al. 2019b. *MNRAS* 489:1919–26
Troja E, van Eerten H, Zhang B, et al. 2020. *MNRAS* 498:5643–51
Utsumi Y, Tanaka M, Tominaga N, et al. 2017. *Publ. Astron. Soc. Jpn.* 69:101
Valenti S, Sand DJ, Yang S, et al. 2017. *Ap. J. Lett.* 848:L24
van de Voort F, Quataert E, Hopkins PF, Kereš D, Faucher-Giguère CA. 2015. *MNRAS* 447:140–48
Villar VA, Cowperthwaite PS, Berger E, et al. 2018. *Ap. J. Lett.* 862:L11
Villar VA, Guillochon J, Berger E, et al. 2017. *Ap. J. Lett.* 851:L21
Wallner A, Faestermann T, Feige J, et al. 2015. *Nat. Commun.* 6:5956
Wanajo S, Sekiguchi Y, Nishimura N, et al. 2014. *Ap. J. Lett.* 789:L39
Wanderman D, Piran T. 2015. *MNRAS* 448:3026–37
Wang H, Giannios D. 2021. *Ap. J.* 908:200
Wang L, Wheeler JC. 2008. *Annu. Rev. Astron. Astrophys.* 46:433–74
Watson D, Hansen CJ, Selsing J, et al. 2019. *Nature* 574:497–500
Waxman E, Ofek EO, Kushnir D, Gal-Yam A. 2018. *MNRAS* 481:3423–41
Wei JJ, Zhang BB, Wu XF, et al. 2017. *J. Cosmol. Astropart. Phys.* 2017:035
Wollaeger RT, Korobkin O, Fontes CJ, et al. 2018. *MNRAS* 478:3298–334
Wu MR, Barnes J, Martínez-Pinedo G, Metzger BD. 2019. *Phys. Rev. Lett.* 122:062701
Wu Y, MacFadyen A. 2019. *Ap. J. Lett.* 880:L23
Xie X, Zrake J, MacFadyen A. 2018. *Ap. J.* 863:58
Yang B, Jin ZP, Li X, Covino S, Zheng XZ, et al. 2015. *Nat. Commun.* 6:7323
Yang S, Valenti S, Cappellaro E, et al. 2017. *Ap. J. Lett.* 851:L48
Zhang B. 2019. *Front. Phys.* 14:64402
Zhang BB, Zhang B, Sun H, et al. 2018. *Nat. Commun.* 9:447
Zhu Y, Wollaeger RT, Vassh N, et al. 2018. *Ap. J. Lett.* 863:L23
Zrake J, Xie X, MacFadyen A. 2018. *Ap. J. Lett.* 865:L2

Annual Review of Astronomy and Astrophysics

Volume 59, 2021

Contents

Indexes

Errata

An online log of corrections to *Annual Review of Astronomy and Astrophysics* articles may be found at http://www.annualreviews.org/errata/astro